SIZES, HALF-MASS DENSITIES, AND MASS FUNCTIONS OF STAR CLUSTERS IN THE MERGER REMNANT NGC 1316: CLUES TO THE FATE OF SECOND-GENERATION GLOBULAR CLUSTERS[1]

Paul Goudfrooij

Space Telescope Science Institute, 3700 San Martin Drive, Baltimore, MD 21218

ABSTRACT

We study mass functions of globular clusters derived from *HST/ACS* images of the early-type merger remnant galaxy NGC 1316 which hosts a significant population of metal-rich globular clusters of intermediate age (~ 3 Gyr). For the old, metal-poor ('blue') clusters, the peak mass of the mass function $\mathcal{M}_p$ increases with internal half-mass density ρ_h as $\mathcal{M}_p \propto \rho_h^{0.44}$ whereas it stays approximately constant with galactocentric distance R_{gal}. The mass functions of these clusters are consistent with a simple scenario in which they formed with a Schechter initial mass function and evolved subsequently by internal two-body relaxation. For the intermediate-age population of metal-rich ('red') clusters, the faint end of the previously reported power-law luminosity function of the clusters with $R_{gal} > 9$ kpc is due to many of those clusters having radii *larger than the theoretical maximum value imposed by the tidal field of NGC 1316* at their R_{gal}. This renders disruption by two-body relaxation ineffective. Only a few such diffuse clusters are found in the inner regions of NGC 1316. Completeness tests indicate that this is a physical effect. Using comparisons with star clusters in other galaxies and cluster disruption calculations using published models, we hypothesize that most red clusters in the low-ρ_h tail of the initial distribution have already been destroyed in the inner regions of NGC 1316 by tidal shocking, and that several remaining low-ρ_h clusters will evolve dynamically to become similar to 'faint fuzzies' that exist in several lenticular galaxies. Finally, we discuss the nature of diffuse red clusters in early-type galaxies.

Subject headings: galaxies: star clusters — globular clusters: general — galaxies: individual (NGC 1316) — galaxies: interactions

1. INTRODUCTION

Globular star clusters (GCs) have long been recognized as important laboratories in the study of the formation and evolution of galaxies for a variety of reasons. Studies of star formation within molecular clouds using infrared observations have shown that most, if not all, stars form in clusters with initial masses $\mathcal{M}_{cl,0}$ in the range $10^2 - 10^8$ $M_\odot$ (e.g., Lada & Lada 2003; Portegies Zwart et al. 2010, and references therein). While most star clusters with $\mathcal{M}_{cl,0} \lesssim 10^4$ $M_\odot$ are thought to disperse into the field population of galaxies within a few Gyr by a variety of disruption processes, the surviving massive GCs constitute luminous compact sources that can be easily observed out to distances of several tens of megaparsecs. Furthermore, star clusters represent very good approximations of a "simple stellar population" (hereafter SSP), i.e., a coeval population of stars with a single metallicity, whereas the diffuse light of galaxies is typically composed of a mixture of populations. Thus, star clusters represent invaluable probes of the SFR and chemical enrichment occurring during the main star formation epochs within a galaxy's assembly history.

As to the class of "normal" giant early-type galaxies (E and S0 galaxies, i.e., galaxies whose light is dominated by a "bulge" component), deep imaging studies with the *Hubble Space Telescope (HST)* revealed that such galaxies typically contain rich GC systems with bimodal color distributions (Kundu & Whitmore 2001; Larsen et al. 2001; Peng et al. 2006a). Follow-up spectroscopy with 8-m class telescopes showed that both "blue" and "red" GC subpopulations are

nearly universally old, with ages $\gtrsim 8$ Gyr (e.g. Forbes et al. 2001; Puzia et al. 2005, 2006; Woodley et al. 2009), similar to the case of GCs in our Galaxy (Marín-Franch et al. 2009). This implies that the color bimodality is due mainly to differences in metallicity. The colors and spatial distribution of the blue GCs are usually consistent with those of metal-poor halo GCs in our Galaxy and M31, while red GCs have colors and spatial distributions that are similar to those of the "bulge" light of their host galaxies (Geisler et al. 1996; Forbes et al. 1997; Rhode & Zepf 2001; Goudfrooij et al. 2001b; Jordán et al. 2004; Peng et al. 2006a; Goudfrooij et al. 2007). Thus, the nature of the red metal-rich GCs is likely to hold important clues to the star formation history of their host galaxies.

The star formation activity associated with the formation of the bulge component of giant early-type galaxies is generally thought to be dominated by vigorous starbursts triggered by mergers and interactions of gas-rich galaxies (e.g., White & Frenk 1991; Baugh et al. 1996; Mihos & Hernquist 1996; Cole et al. 2000; Somerville et al. 2001). Indeed, deep images taken with the *HST* have shown that nearby galaxy mergers and young merger remnant galaxies host very rich populations of young star clusters with masses reaching 10^7 $M_\odot$ and beyond (e.g., Holtzman et al. 1992; Schweizer et al. 1996; Miller et al. 1997; Whitmore et al. 2010). The ages and masses of these young clusters predicted from their colors and luminosities were confirmed by spectroscopy (Zepf et al. 1995; Schweizer & Seitzer 1998; Maraston et al. 2004; Bastian et al. 2006). Their metallicities tend to be near-solar, as expected for clusters formed out of enriched gas in spiral galaxies. As to the question whether or not these young metal-rich GC populations can survive several Gyr of stellar and/or dynamical evolution (this was brought up by Brodie et al. 1998), studies of GCs in early-type merger remnants of intermediate age ($2-4$ Gyr) have shown that such metal-rich

GC populations do survive at least that long with relatively minor changes in their mass function down to the detection limit (Goudfrooij et al. 2001a,b; Whitmore et al. 2002; Goudfrooij et al. 2004, 2007). It seems natural to interpret these data in the sense that the bulges of normal giant early-type galaxies and their metal-rich GCs formed at high redshift in a way similar to that observed in gas-rich galaxy mergers today, as originally predicted by Schweizer (1987) and Ashman & Zepf (1992).

A significant difference between young GC systems in mergers and ancient GC systems is the shape of their respective luminosity functions (LFs). Young GC systems in mergers and young merger remnants have LFs consistent with power laws: $\phi(L) \propto L^{\alpha}$ with $\alpha \simeq -2$ (e.g., Schweizer et al. 1996; Miller et al. 1997; Zepf et al. 1999; Zhang & Fall 1999; Fall et al. 2009), without a sign of a peak or "turnover" down to the detection limit of the data. Perhaps not surprisingly, this distribution is consistent with the mass function of giant molecular clouds in star forming regions in our Galaxy (Elmegreen & Efremov 1997). In contrast, the LFs of GC systems in "normal" galaxies are well described by Gaussians in magnitude space (or lognormal luminosity distributions), peaking at $M_V^0 \simeq -7.4$ mag (e.g., Harris 2001; Jordán et al. 2007), corresponding roughly to a "turnover" mass $\mathcal{M}_{TO} \simeq 1.5 \times 10^5$ M$_{\odot}$. If one accepts the view that ancient GCs in normal galaxies formed in the early universe through essentially the same processes as star clusters in galaxy mergers today, then large numbers of low-mass clusters must have been destroyed or disrupted in the mean time. Recent studies of dynamical evolution of GCs through mechanisms acting on long time scales (notably two-body relaxation and tidal shocking) have shown that low-mass clusters disrupt first as galaxies age, which can evolve a power-law mass function into lognormal mass functions in a few Gyr (e.g., Fall & Rees 1977; Fall & Zhang 2001; Prieto & Gnedin 2008, but see Vesperini 2001). However, there is some debate as to the impact of the tidal field of the host galaxy on the way GC mass functions (GCMFs) are shaped over time. One school of thought is that long-term cluster disruption is dominated by *internal* two-body relaxation which is essentially independent of the tidal field of the galaxy. This view is supported by properties of the GCMFs of the Milky Way and the Sombrero galaxy (Chandar et al. 2007; McLaughlin & Fall 2008). Another view is that the strength of the tidal field must be a significant factor in terms of the impact of two-body relaxation (e.g. Baumgardt & Makino 2003; Gieles & Baumgardt 2008; Baumgardt et al. 2008). This in turn seems to be supported by the finding that the turnover luminosity of GCLFs of early-type galaxies decreases with decreasing galaxy luminosity (Jordán et al. 2007). Studies of GC systems of intermediate-age ($1 - 5$ Gyr old) merger remnants can help clarify the relative importance of different dynamical effects on GC systems formed during galaxy interactions.

Several studies have established firmly that the giant galaxy NGC 1316 (= Fornax A = Arp 154), the dominant galaxy of a subgroup of the Fornax cluster of galaxies, is a *bona fide* intermediate-age merger remnant. Its outer envelope includes several nonconcentric arcs, tails, and loops that are most likely remnants of tidal perturbations, while the inner part of the spheroid is characterized by a surprisingly high central surface brightness and small effective radius for the galaxy's luminosity (Schweizer 1980, 1981; Caon et al. 1994). All of these features indicate that NGC 1316 is the product of a dis-

sipative merger with incomplete dynamical relaxation. Goudfrooij et al. (2001a,b) discovered a significant population of $\simeq 3$-Gyr-old GCs of near-solar metallicity through a comparison of *BVIJHK* colors as well as Hα and Ca II triplet line strengths with SSP model predictions. It is classified as a lenticular galaxy in galaxy catalogs: (R')SAB(s)0 in the RC3 catalog (de Vaucouleurs et al. 1991) and S0$_1$pec in the RSA catalog (Sandage & Tammann 1987), and its stellar body is rotationally supported (e.g., Arnaboldi et al. 1998). In accordance with our earlier work, we adopt a distance of 22.9 Mpc for NGC 1316 in this paper. This distance was derived using known tight relations between the light curve shape, luminosity, and color of type Ia supernovae in NGC 1316 (see Goudfrooij et al. 2001b, and references therein).

In a previous paper (Goudfrooij et al. 2004), we used deep photometry taken with the Advanced Camera for Surveys (ACS) aboard *HST* and showed that the inner 50% of the system of intermediate-age GCs of NGC 1316 showed evidence of the presence of a turnover in its LF, while the GCLF of the outer 50% was still consistent with a power-law down to the detection limit. While this provided evidence that long-term dynamical evolution of GCs formed in mergers of massive gas-rich galaxies can indeed transform MFs of "young" clusters to MFs of ancient GC systems, it did not clarify the fate of the clusters in the outer regions of NGC 1316. A specific issue in that regard is that GCLFs and GCMFs in the outskirts of "normal" galaxies typically show very similar shapes and turnovers to those in their inner regions, and the question is whether and how dynamical evolution of the GCs in the outskirts of NGC 1316 may create a mass function similar to those seen in "normal" giant early-type galaxies over the next ~ 10 Gyr. Using new GC size measurements, this issue is one of the main topics being addressed in the current paper.

The remainder of this paper is organized as follows. After a brief description of the imaging data in Section 2, the data analysis is presented in Section 3. Section 4 describes relations between radii and other properties of the blue and red GC subpopulations in NGC 1316 and presents their mass functions as functions of mass density and galactocentric radius. In Section 5, we apply various dynamical evolution model calculations to the red, intermediate-age clusters and evaluate the properties of their resulting mass functions and their distribution in the mass-radius plane. A summary and discussion of the results, including the large number of diffuse red clusters in NGC 1316, is provided in Section 6.

2. DATA

We use the *HST/ACS* imaging dataset described previously in Goudfrooij et al. (2004). Briefly, this consists of several wide-field channel (WFC) images taken with the F435W, F555W, and F814W filters with total exposure times of 1860 s, 6980 s, and 4860 s, respectively. The sample of star cluster candidates in NGC 1316 and its subdivision in "old, metal-poor" ("blue") versus "intermediate-age, metal-rich" ("red") clusters was adopted from Goudfrooij et al. (2004). For purposes of dynamical evolution calculations, we assume throughout this paper that the system of "red" GCs in NGC 1316 is dominated by GCs of an age of 3 Gyr, which is the age found for the brightest red GCs using spectroscopy and multi-color photometry (Goudfrooij et al. 2001a,b). While it is possible that (one of) the progenitor galaxies possessed older metal-rich GCs that were "donated" to NGC 1316 during the merger, the LF of the red GCs does not show any sign of the presence of a significant number of

"old" GCs such as a turnover near $M_V^0 \simeq -7.4$ mag (see Goudfrooij et al. 2004). Instead, the LF of the red GCs continues to rise to the completeness limit of the data similar to the situation in other merger remnants. Hence we deem it unlikely that NGC 1316 hosts *significant* numbers of old red GCs formerly associated with merger progenitor galaxies. However, the impact of the presence of a small fraction of old metal-rich GCs to the results shown in this paper will be discussed where relevant.

3. ANALYSIS

3.1. *Size Measurements*

GC structural parameters were derived using the ISHAPE algorithm (Larsen 1999), which fits the object's surface brightness profile with analytical models convolved with a subsampled PSF. Since GCs at the distance of NGC 1316 are only marginally resolved, reliable size measurements require a very good knowledge of the ACS PSF at the time of observation. While many studies build empirical PSFs from several well-exposed stars in the field of view for this purpose, the ACS images of NGC 1316 do not contain enough such stars to create a robust set of PSFs. Hence we have to rely on external PSF libraries. To test the influence of the PSF library chosen, we performed a comparison between r_h values measured using PSFs created by means of two methods: *(i)* the TINYTIM package (Krist & Hook 2004) which takes into account the field-dependent aberration of the ACS/WFC camera, filter passband effects, charge diffusion variations, and varying pixel area due to the significant field distortion in the ACS/WFC field of view. The ten times subsampled Tiny Tim PSF was evaluated at the position of each point-like object in the image and convolved with the charge diffusion kernel. *(ii)* the empirical grid of ACS PSFs of Anderson & King (2006). Since the latter PSFs are created for individual ACS *_flt.fits images rather than images combined with MULTIDRIZZLE, we used Maurizio Paolillo's *Multiking* suite of scripts (which we modified to work on filters other than F606W) to create a grid of empirical PSFs at the location of each GC candidate in blank versions of each individual input _flt.fits ACS image. These images were then combined by MultiDrizzle in the exact same way as the final NGC 1316 image. These PSFs were then subsampled by a factor 10 in order for them to be used appropriately within ISHAPE, using polynomial interpolation. We refer to these PSFs as *ePSFs* in the following discussion. These two sets of PSFs were then used within ISHAPE to fit the objects' profiles with King (1962) model concentration parameters $C_K \equiv r_t/r_c$ (where r_t is the tidal radius and r_c is the core radius) of 5, 15, 30, and 100. GC structural parameters were calculated using the C_K value that yielded the lowest χ^2.

The effect of the fitting radius (parameter FITRAD within ISHAPE) on the derived cluster radii was assessed by using values of 4, 6, 10, and 15 pixels. While larger values of FITRAD are in principle preferable over smaller ones (especially for more extended sources), we found that the associated increase in fitting uncertainties for fainter sources renders this advantage negligible. Similar to Carlson & Holtzman (2001), we find that FITRAD $\geq$ 6 pixels yield consistent r_h values within the uncertainties, even for the largest GCs found in this study (which are mainly the fainter ones, see Sect. 4.2 and beyond). Hence we adopt FITRAD = 6 pixels for this study. GC half-light radii r_h were derived from the geometric mean of the FWHM values measured along the semi-major and semi-
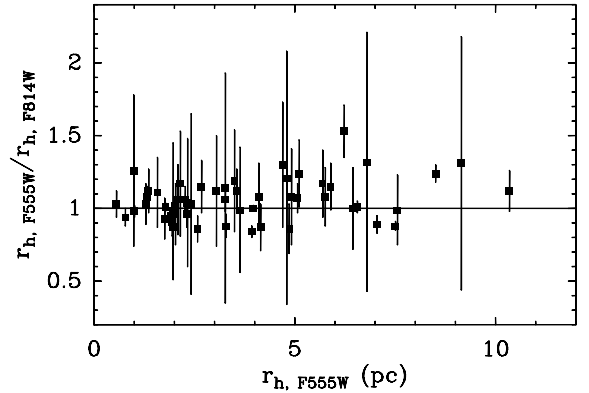

FIG. 1.— $r_{h,F555W}/r_{h,F814W}$ (the ratio of r_h values measured in the F555W and F814W passbands) vs. r_h in F555W for all GC candidates with S/N $\geq$ 50 in both passbands. The solid line indicates a ratio of unity. Error bars are only shown for $r_{h,F555W}/r_{h,F814W}$ to avoid clutter. There does not seem to be a significant systematic difference between r_h values measured in F555W and F814W.

minor axes. The measured values of r_h were multiplied by a factor 4/3 to account for projection effects (Spitzer 1987). In order to render correct values of signal-to-noise ratio (S/N) for the fits, we added the local background level back into the model-subtracted image (using the MKNOISE task within IRAF) for each object prior to running ISHAPE on it. Objects fit by ISHAPE with S/N $\geq$ 50 were considered for the remaining analysis. Several studies found this S/N constraint sufficient to yield reliable half-light radii when using methods such as ISHAPE (e.g., Larsen 1999; Harris 2009; T. H. Puzia et al. 2012, in preparation)[2].

To test for systematic differences between sizes measured in the F555W and F814W images, we plot the ratio $r_{h,F555W}/r_{h,F814W}$ versus $r_{h,F555W}$ in Figure 1 for all clusters measured with S/N $\geq$ 50 in both passbands. Weighting by inverse variance, the weighted mean value $\langle r_{h,F555W}/r_{h,F814W}\rangle = 0.98 \pm 0.02$. We thus assume that there is no significant systematic difference between sizes measured in F555W versus F814W for this dataset. In the following, we concentrate on sizes measured in the F555W image because *(i)* the F555W image reaches the highest S/N ratio for cluster candidates in the color parameter space of interest and *(ii)* F555W images were taken using the highest number of distinct spatial offsets (6 "dithers") between individual images which renders the highest spatial resolution after image combination using the MULTIDRIZZLE task available within PyRAF/STSDAS. The constraint of S/N $\geq$ 50 in the F555W image yielded a total of 424 GCs, 212 of which are "red" and 212 are "blue". Fig. 2 depicts a comparison between the r_h values derived from the best-fit TINYTIM PSFs and those derived from the *ePSFs*. The r_h values derived from the *ePSFs* are systematically smaller than those derived from the TINYTIM PSFs by 0.45 ± 0.05 pixel. Effects of this order of magnitude (differences of 0.4 – 0.5 pixel) were also seen in previous studies using *HST/ACS* images that compared GC sizes derived with TINYTIM PSFs versus empirical PSFs (e.g., Spitler et al. 2006; Georgiev et al. 2009). This discrepancy is likely due to effects that are not incorporated in TINYTIM such as telescope focus changes among and during *HST* orbits ("breathing") as well as slight broadening of the effective PSF due to

---

[2] We note that a much higher value of S/N is required to determine King model concentration indices robustly for marginally resolved objects (S/N $\gtrsim$ 150, see Carlson & Holtzman 2001). Hence, the best-fit values of C_K determined here for each GC should typically be regarded as estimates.
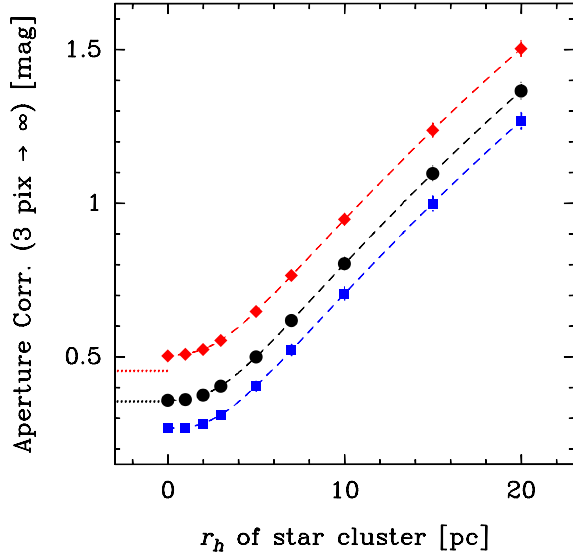
FIG. 2.— Comparison between r_h values of GC candidates in NGC 1316 derived using PSFs from *ePSF* (abscissa) and TINYTIM. The solid line depicts a 1:1 relation, while the dashed line shows the best-fit line to the data.
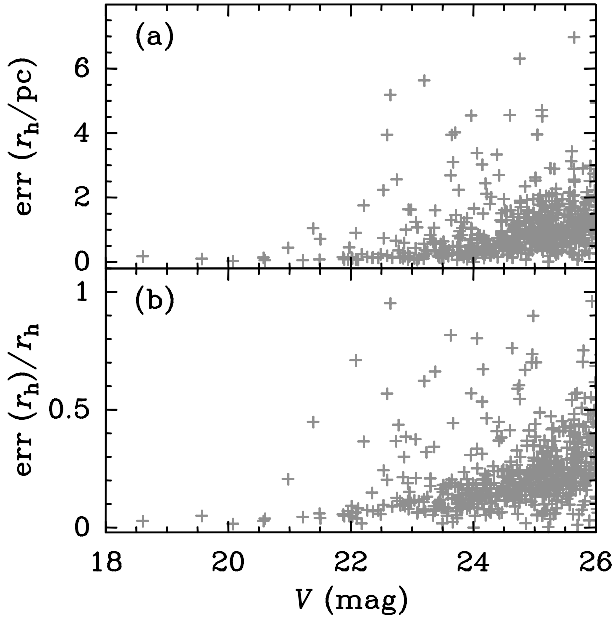

FIG. 3.— *Panel (a)*: err (r_h) (the standard deviation of r_h) versus V magnitude for GC candidates with size measurements from the F555W image. *Panel (b)*: err $(r_h)/r_h$ versus V magnitude for the same objects.

the effect of image combination. With this in mind, we adopt the structural parameters of GCs measured using the *ePSF*s.

Finally, Figure 3 depicts the formal standard deviation of r_h as a function of magnitude calculated from the ISHAPE output, both in an absolute sense and relative to the values of r_h. Standard deviations were calculated using ISHAPE parameter CORRERR = YES, meaning that correlated errors between different ISHAPE parameters were taken into account. Table 1 lists magnitudes, colors, r_h values, and C_K values for all GC candidates used in this paper.

3.2. *Impact of Varying Cluster Size to Observables*

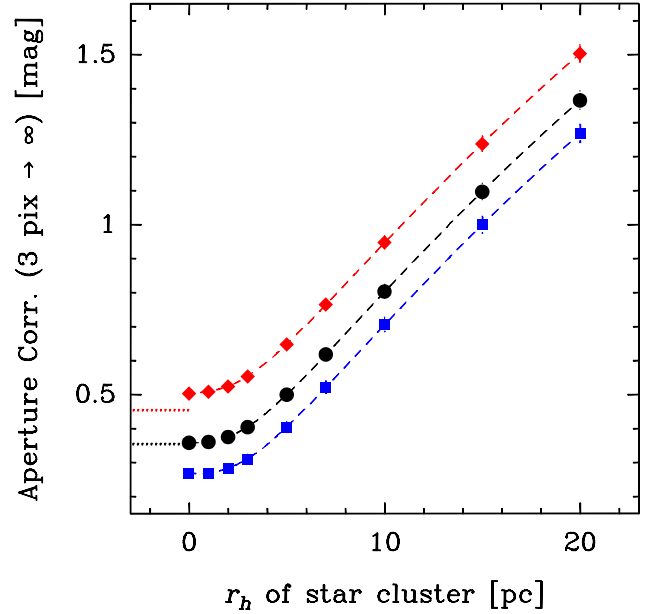#### 3.2.1. *Aperture Corrections*

FIG. 4.— Aperture correction from a measurement radius of 3 pixels to "infinity" as a function of star cluster half-light radius r_h at the distance of NGC 1316. Squares represent F435W data, circles represent F555W data, and diamonds represent F814W data. For visualization purposes, the F555W and F814W data are offset from the F435W data in the Y direction by +0.1 and +0.2 mag, respectively. These offsets are indicated by dotted lines near the bottom left of the plot. Dashed lines indicate polynomial fits to the data. Note the significant increase of aperture corrections for clusters with $r_h \gtrsim 4$ pc. See § 3.2.1.

The effect of varying GC sizes to photometric aperture corrections at the distance of NGC 1316 was determined by using the *Multiking* package (see § 3.1 above) to create a grid of *ePSF*-convolved King (1962) models located uniformly throughout the ACS/WFC field of view for all three ACS/WFC filters used in this dataset. In this regard we used r_h values of 0, 1, 2, 3, 5, 7, 10, 15, and 20 pc and King concentration parameters $C_K = 5$, 15, 30, and 100. Aperture corrections were calculated from an aperture radius of 3 pixels (as used by Goudfrooij et al. 2004 for example) to 50 pixels. We found that the effect of varying C_K to these aperture corrections at a given r_h was negligible relative to the effect of varying r_h itself. The aperture corrections for the various r_h values are plotted in Fig. 4. Note that the total intensities of the *ePSF*'s are normalized to unity within a radius of 10 ACS/WFC pixels (Anderson & King 2006). Hence, the aperture correction values from a radius of 10 pixels to infinity listed by Sirianni et al. (2005) were added to the measured values to arrive at the "final" aperture correction values plotted in Fig. 4. Aperture corrections for all clusters were applied by means of 5th-order polynomial least-square fits of aperture correction versus r_h. These fits are shown in Fig. 4 as dashed lines.

Note the significant increase of aperture correction values for clusters with $r_h \gtrsim 4$ pc, which has a relevant impact on such clusters' derived luminosities and masses when compared with "average-sized" clusters which have $1 \lesssim r_h/\text{pc} \lesssim 4$. This turns out to have a significant impact for the case of NGC 1316: The clusters used by Goudfrooij et al. (2004) to calculate aperture corrections were the 35 brightest clusters (with $V \leq 23.0$ mag). While those clusters obviously render the highest-quality aperture corrections as intended, it turns out that their r_h distribution is not representative for the cluster system as a whole. This is illustrated in Fig. 5: Clusters with $r_h \gtrsim 4$ pc are quite common among the cluster system as

TABLE 1
PHOTOMETRY, ASTROMETRY, AND SIZES OF GC CANDIDATES IN NGC 1316[a].

ID (1)	ID$_{2001b}$ (2)	RA (3)	DEC (4)	V (5)	V−I (6)	r_h (7)	C_K (8)
1	114	50.6770102	−37.2111334	18.607 ± 0.002	1.093 ± 0.002	6.23 ± 0.18	30
2		50.6781450	−37.2045648	19.570 ± 0.002	1.013 ± 0.002	2.03 ± 0.10	30
3	210	50.6585913	−37.2186257	20.078 ± 0.002	1.003 ± 0.002	1.70 ± 0.03	30
4	110	50.6522255	−37.1822058	20.578 ± 0.004	1.044 ± 0.006	4.74 ± 0.14	30
5		50.6923963	−37.2013999	20.601 ± 0.004	1.055 ± 0.006	1.40 ± 0.05	30

NOTE. — Column (1): Object ID (sorted by V magnitude). (2): Object ID in Goudfrooij et al. (2001b). (3) and (4): Right ascension (RA) and Declination (DEC) (both in degrees) in J2000 equinox. For reference, the coordinates of the center of NGC 1316 on the F555W ACS image is (RA, DEC) = (50.6739027, −37.2079400). (5): V mag (Vega-based). (6): V−I color in mag. (7): Measured half-light radius in pc. (8): King concentration index yielding the lowest χ^2.

[a]Table 1 is published in its entirety in the electronic edition of *The Astrophysical Journal*. A portion is shown here for guidance regarding its form and content.
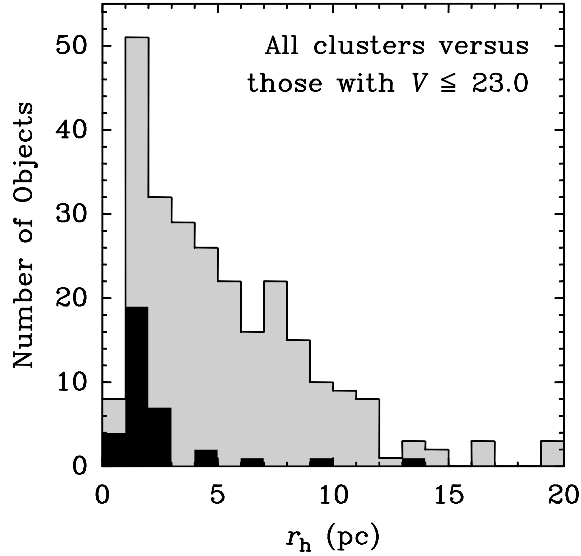

FIG. 5.— Distributions of half-light radii for all star clusters in NGC 1316 with reliable size measurements (light-grey histogram) and for the star clusters with V ≤ 23 mag (black histogram). Note that the latter distribution misrepresents the former for $r_h \gtrsim 4$ pc. I.e., average aperture corrections derived from the brightest clusters yield significantly underestimated aperture corrections for clusters with $r_h \gtrsim 4$ pc.

a whole (see also Masters et al. 2010) whereas they happen to be strongly underrepresented among clusters with V ≤ 23.0 mag. Obviously, the measurement of half-light radii can be very important in photometry studies of star clusters that are marginally resolved (see also Kundu 2008).

3.2.2. *Completeness Corrections*

Given the varying cluster sizes and their possible systematics with galactocentric distance, we investigated the influence of varying cluster sizes to completeness corrections by repeating the artificial object tests done in Goudfrooij et al. (2004), but now using the *Multiking* package to add simulated GCs with r_h = 1, 2, 3, 5, 7, 10, 15, and 20 pc and C_K = 30 to the final NGC 1316 images in the F555W and F814W filters. The background levels and (total) magnitude intervals employed for the completeness tests were identical to those used in Goudfrooij et al. (2004), as were the parameters used for the DAOFIND task within IRAF. The resulting completeness functions and their dependence on GC size are illustrated in Fig. 6 for a typical background level of 200 e⁻/pix per individual 1100 s exposure.

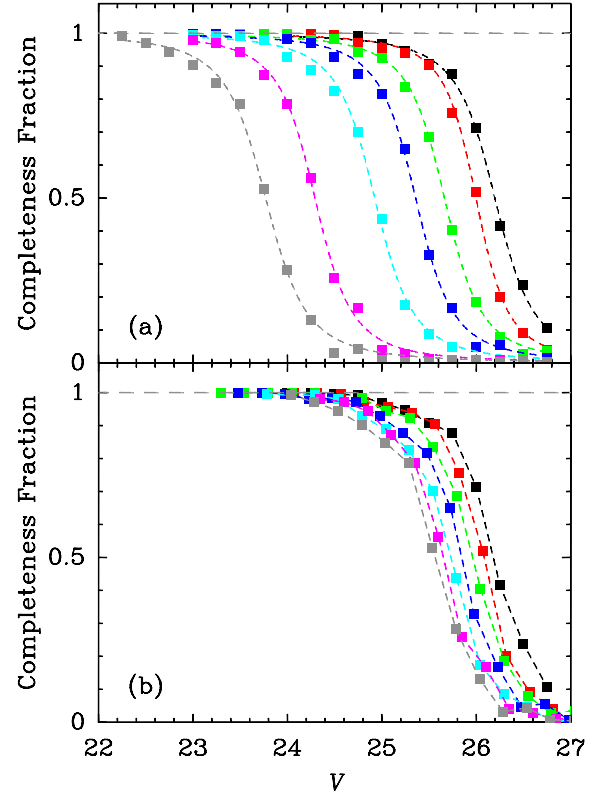Completeness values were parameterized by fitting the

FIG. 6.— Completeness functions for the ACS photometry of star clusters in NGC 1316 as function of *total* magnitude and r_h. A typical background level of 200 e⁻/pix was used for this example. *Panel (a)*: Completeness fractions for r_h values (in pc) of 2 (black symbols), 3 (red), 5 (green), 7 (blue), 10 (cyan), 15 (magenta), and 20 (grey). The dashed lines depict the completeness function (equation 1) fit to the data. *Panel (b)*: Same data as in panel (a), but now the magnitudes for r_h > 2 pc have been shifted by the difference in aperture corrections between that for the r_h value in question and that for r_h = 2 pc. See discussion in Sect. 3.2.2.

measured completeness fractions $f(V)$ by the following function:

$$f(V) = \frac{1}{2}\left(1 - \frac{\alpha_c(V - V_{\mathrm{lim}})}{\sqrt{1 + \alpha_c^2(V - V_{\mathrm{lim}})^2}}\right), \qquad (1)$$

where V_{lim} is the 50% completeness limit in V and the parameter α_c is a measure of the steepness of the completeness function near V_{lim}. Panel (a) of Fig. 6 depicts the curves $f(V)$ that were fit to the simulated data of the various r_h values mentioned above, using a least-squares fitting routine to determine α_c and V_{lim}. These fits were performed for 5 background

levels encompassing the observed values, equally spaced in $\log(\text{background})$. Completeness fractions of all individual clusters were then determined from their V magnitudes, background levels, and r_{h} values. Values for α_{c} and V_{lim} in the function $f(V)$ were determined by means of bilinear interpolation in $\log(\text{background})$ versus $\log(r_{\text{h}})$ parameter space.

As shown by panel (a) of Fig. 6, the dependence of the completeness fraction on half-light radius is significant. In quantitative terms, V_{lim} ranges from 26.2 for $r_{\text{h}} = 2$ pc to 23.8 for $r_{\text{h}} = 20$ pc, roughly by 2.4 mag per dex in r_{h}. However, when comparing this result to the completeness values used in Goudfrooij et al. (2004), one should keep in mind that Goudfrooij et al. (2004) used a cluster profile based on the brightest 35 clusters for their artificial objects. That cluster profile had a $r_{\text{h}} \simeq 2$ pc (see Fig. 5). Since the brightness of artificial objects is scaled by their *total* (integrated) magnitude prior to being inserted in an image while the photometric measurements are done with an aperture radius of 3 pixels (both here and in Goudfrooij et al. 2004), a proper comparison between the completeness values determined in this paper versus those in Goudfrooij et al. (2004) should take the aperture corrections for clusters of different sizes into account. Hence we shift the magnitudes in panel (a) of Fig. 6 by the size-dependent aperture correction values shown in Fig. 4, relative to those appropriate for $r_{\text{h}} = 2$ pc. The result is shown in panel (b) of Fig. 6. Note that the "net" size dependence of completeness values is much reduced relative to the results shown in panel (a): V_{lim} effectively changes by only 0.6 mag per dex in r_{h}.

3.3. *Contamination by Background Galaxies*

Contamination by compact background galaxies is always a potentially critical issue in extragalactic star cluster studies. To address this, we select images from 4 blank, high-latitude control fields that used ACS/WFC over the course of 3 HST orbits ($\simeq 2.3$ hours) with the F555W and F814W filters from the HST archive. These observations were taken as parallel images in HST Program GO-11691, and are well suited to the purpose of probing the background contamination in our cluster sample. Each of these sets of images were then run through the same image combination, object detection and selection, and aperture photometry procedures as those employed by Goudfrooij et al. (2004) for the NGC 1316 images, with one exception. Since none of these control fields included large foreground galaxies, the compact-source photometry in these control fields goes deeper than in the NGC 1316 images. Hence we performed the detection of cluster candidates as if NGC 1316 were included in each blank field. To this end, we used the "model" images generated during the object detection procedure for the NGC 1316 images (see Goudfrooij et al. 2004) from which we calculated images representing the Poisson noise associated with the diffuse light of NGC 1316, using the MKNOISE program within IRAF. The latter noise images were added to the blank fields (after scaling by the square root of the exposure times) prior to running the detection procedure.

The level of background contamination of the "blue" and "red" cluster subsamples is illustrated in Figure 7 which shows size-magnitude diagrams for the data and control fields. The top panels show "blue" candidate clusters while the bottom panels show "red" candidate clusters. The control field photometry tables have been randomly sampled so as to only plot 1/4 of the objects found in the 4 blank fields. Typically, the relatively small number of "cluster candidates" found in the control fields (which are most likely background galaxies)

are fainter and more extended than the (far more numerous) cluster candidates in the NGC 1316 images.

To evaluate the probability that a given cluster candidate in the NGC 1316 images is physically associated with NGC 1316, we apply a two-dimensional Gaussian smoothing kernel to the data in $\log(r_{\text{h}})$ versus V parameter space to produce density distributions of the numbers of cluster candidates and contaminants per unit area using the KDE2D algorithm (Venables & Ripley 2002). Probability values $p = p(\log(r_{\text{h}}), V)$ for cluster candidates being physically associated with NGC 1316 are then calculated from the ratio $F_{\text{N1316}}/F_{\text{blank}}$ where F_{N1316} and F_{blank} are the two-dimensional density distributions of cluster candidates in NGC 1316 and in the blank fields, respectively. For the remainder of this paper, we define "clusters" as objects with $p \geq 0.67$, i.e., objects with $F_{\text{N1316}} \geq 2 \times F_{\text{blank}}$.

4. SIZE DEMOGRAPHY OF THE CLUSTER SUBPOPULATIONS

In this Section we illustrate the size-related properties of the metal-poor (blue) and metal-rich (red) cluster subpopulations in NGC 1316 and attempt to put them in context by comparing them to clusters in our Galaxy, younger merger remnant galaxies, and "normal", old giant early-type galaxies.

4.1. *Dependence on Galactocentric Radius*

The top and middle panels of Fig. 8 plot r_{h} versus projected galactocentric radius R_{gal} for blue and red clusters in NGC 1316. To avoid biases related to varying incompleteness as functions of r_{h} and R_{gal}, only clusters brighter than $V = 25.3$ mag are considered (cf. panel b of Fig. 6). In panel (b) of Fig. 8 we plot running medians of the r_{h} distribution as function on R_{gal}. As can be seen, median sizes of the blue GCs are $\widetilde{r_{\text{h}}} \sim 2.5 - 3.5$ pc with only a slight dependence on R_{gal}. This is similar to the situation seen for metal-poor GCs in "normal" early-type galaxies (e.g., Spitler et al. 2006; Harris 2009; Madrid et al. 2009). However, the situation for the red GCs in NGC 1316 is markedly different from that in "normal" ellipticals. In NGC 1316, the red GCs within ~ 5 kpc from the galaxy center have sizes similar to those of the blue GCs. Outside $R_{\text{gal}} = 5$ kpc however, the median size of the red GCs increases steadily with increasing galactocentric radius, reaching $\widetilde{r_{\text{h}}} \approx 7.5$ pc at $R_{\text{gal}} \sim 12$ kpc. In stark contrast, sizes of red GCs in "normal" ellipticals are typically $\sim 20\%$ *smaller* than blue GCs (e.g., Kundu & Whitmore 1998; Puzia et al. 1999; Jordán et al. 2005; Masters et al. 2010). The size ratio of blue versus red GCs in "normal" ellipticals does not change significantly with R_{gal} (Paolillo et al. 2011; T. H. Puzia et al. 2012, in preparation).

To put this result in context, recall that the bulk of red GCs in NGC 1316 most likely represent an intermediate-age population (age ~ 3 Gyr, cf. Goudfrooij et al. 2001a,b; Bastian et al. 2006). Assuming that to be the case, long-term cluster disruption mechanisms such as two-body relaxation and tidal shocks will have been active for *much* (some $7 - 10$ Gyr) less long than for "old" red GCs in "normal" ellipticals. In particular, late-epoch cluster contraction due to accumulative effects of two-body relaxation (e.g., Mackey et al. 2008; Heggie & Giersz 2008; Vesperini et al. 2009) will not yet have taken place. As such, one might expect the size demography of the red GCs in NGC 1316 to bear similarities to that of younger cluster systems in otherwise similar environments. While size measurements of young GCs in massive merger remnant galaxies are still quite sparse in the literature, the available data do show strong similarities to the red GCs in
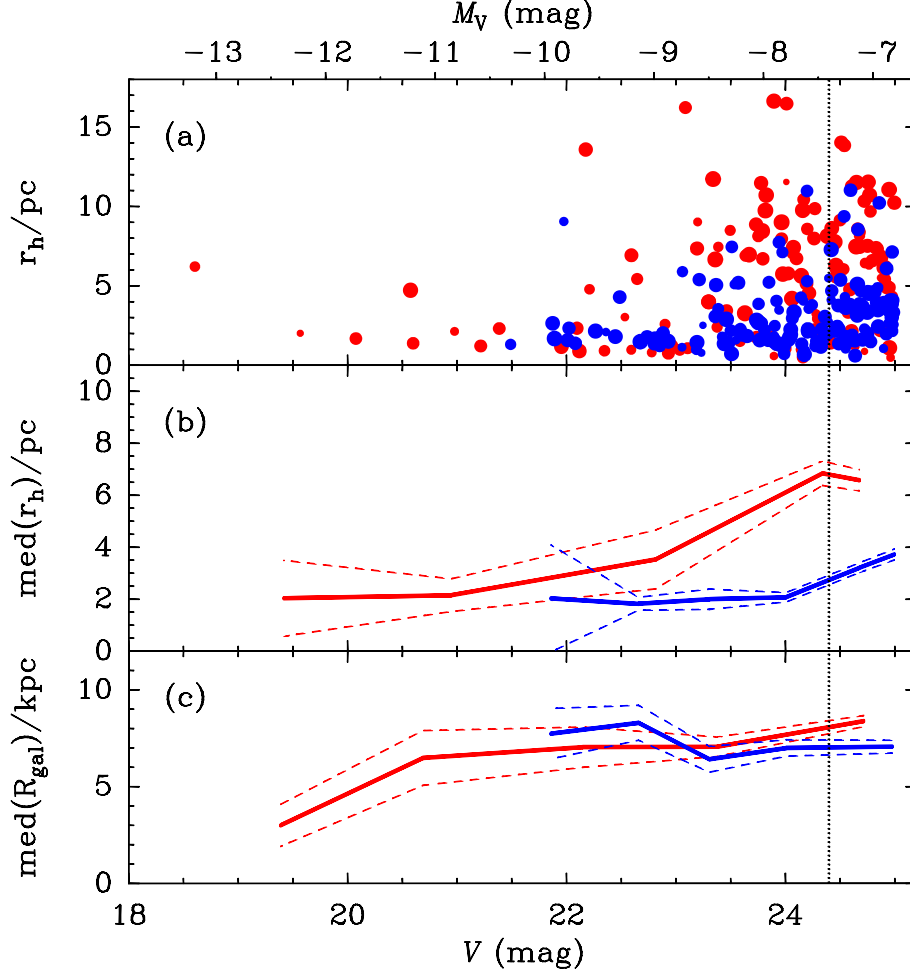
FIG. 7.— Size-magnitude diagrams of cluster candidates in NGC 1316 and blank fields. Panel (a) shows the "blue" (metal-poor) cluster candidates in the NGC 1316 images while panel (b) does so for the "red" (metal-rich) cluster candidates. Panel (c) shows a random selection of 1/4 of the "blue" objects detected in 4 blank sky control fields that were customized for the depth reached in the NGC 1316 image. Panel (d) is similar to panel (c), but now for 2/4 of the "red" objects detected in the 4 control fields (to decrease stochasticity). Symbol colors and types (see boxed-in legends for each pair of panels) reflect the probability p that the object in question is physically associated with NGC 1316. See discussion in Sect. 3.3.

NGC 1316. Trancho et al. (2007) measured half-light radii of $10-20$ pc for young GCs in the outskirts of NGC 3256, a remnant of a recent galaxy merger which Toomre (1977) placed in the middle of his sequence of disk galaxy merger remnants. These clusters in NGC 3256 have estimated ages of $\simeq 100$ Myr (see also Zepf et al. 1999), and hence they have likely already undergone the cluster expansion driven by strong mass loss due to supernova type II explosions as well as stellar evolution in the first few 10^7 yr (Baumgardt et al. 2008; Vesperini et al. 2009), which renders them an appropriate comparison with the intermediate-age red GCs in NGC 1316. Other young cluster systems in merger remnants with accurate size measurements also have size distributions similar to that of the red GCs in NGC 1316, cf. the $\sim 300-700$ Myr old clusters in NGC 1275 and NGC 3597 (Carlson & Holtzman 2001), with mean r_h values of 6.2 and 5.4 pc, respectively, and a set of 8 clusters covering the age range $10 \lesssim$ Age/Myr $\lesssim 700$ in the Antennae galaxies, with a mean r_h of 8.0 pc (Bastian et al. 2009). In conclusion, the relatively large sizes seen among the red GCs in NGC 1316 seem consistent with them being intermediate-age counterparts of metal-rich clusters seen in younger merger remnants. The observed increase of the median r_h of the red GCs with increasing R_{gal} will be discussed below in Sect. 5.

4.2. Luminosity-Radius Relation

Panels (a) and (b) of Fig. 9 plot r_h versus M_V for the same clusters as those shown in Fig. 8. With regard to the blue (metal-poor) GCs, previous studies of sizes of GCs in galaxies found no significant relation between r_h and luminosity down to the turnover of the GC luminosity function (e.g., McLaughlin 2000; Jordán et al. 2005). Our results for the blue GCs are consistent with this. However, our dataset yielded robust r_h values for GCs fainter than the turnover luminosity for old, metal-poor GCs ($M_V = -7.4$; see Fig. 9) where we find evidence for an increase of the (median) size of blue GCs with decreasing luminosity. Panel (c) of Fig. 9 shows that this increase is *not* due to the increase of r_h with increasing R_{gal} for $R_{gal} \gtrsim 11$ kpc for blue GCs shown in Fig. 8. Instead, we interpret this effect as being due to dynamical evolution *within* GCs, i.e. the mass density dependence of cluster evaporation due to two-body relaxation, as discussed further in Sect. 4.3 below.

As to the red (metal-rich) GCs, panel (b) of Fig. 9 shows an obvious increase of r_h with decreasing luminosity. However, before trying to interpret this relation in terms of physical effects, we point out that it is likely associated with the correlation between r_h and R_{gal} shown in panel (b) of Fig. 8. This is illustrated by panel (c) of Fig. 9 which shows that the
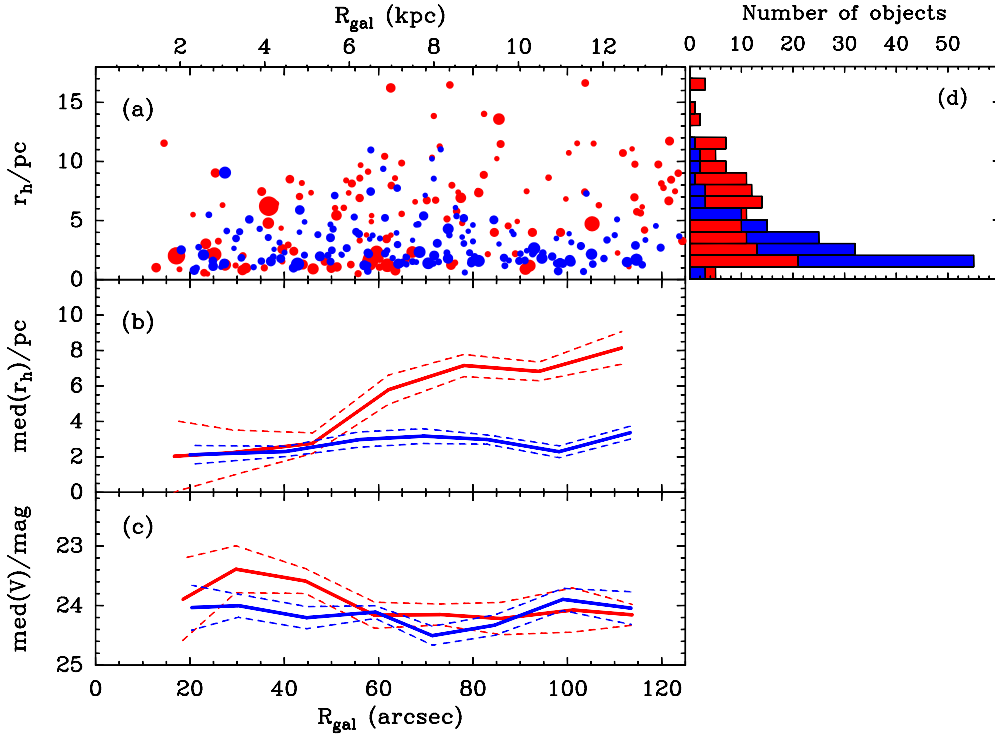
FIG. 8.— *Panel (a)*: GC half-light radius r_h as function of projected galactocentric radius R_{gal} for individual GCs with $V \leq 25.3$ mag. Blue and red symbols or lines represent metal-poor and metal-rich GCs, respectively, for *all* panels. The size of circles scales logarithmically with the GCs' V-band luminosity. *Panel (b)*: Same as panel (a), but now solid lines represent running median values of r_h. Dashed lines mark the $\pm 1\sigma$ error of the mean. *Panel (c)*: Solid lines represent running median values of V magnitude as function of R_{gal}. Dashed lines mark the $\pm 1\sigma$ error of the mean. *Panel (d)*: Distribution of r_h values plotted as histograms. See discussion in Sect. 4.1.
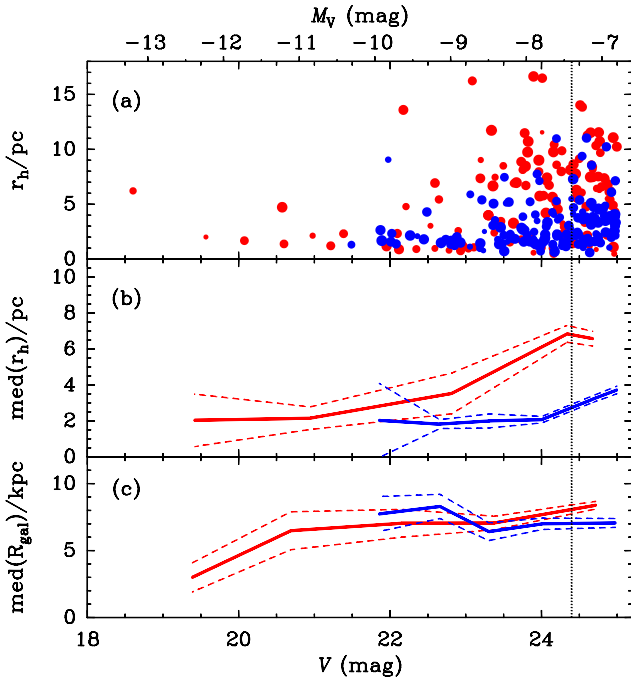

FIG. 9.— *Panel (a)*: GC half-light radius r_h as function of V (or M_V, see top abscissa) for individual GCs with $V \leq 25.3$ mag. Blue and red symbols or lines represent metal-poor and metal-rich GCs, respectively, for *all* panels. The size of the circle scales logarithmically with the GCs' galactocentric radius. *Panel (b)*: Same as panel (a), but now solid lines represent running median values of r_h. Dashed lines mark the $\pm 1\sigma$ error of the mean. *Panel (c)*: Solid lines represent running median values of the galactocentric radius R_{gal} as function of V. Dashed lines mark the $\pm 1\sigma$ error of the mean. The vertical dotted line indicates $M_V = -7.4$, the turnover luminosity for "old", metal-poor GC systems. See discussion in Sect. 4.2.

median R_{gal} also increases significantly with decreasing luminosity. Note that for GCs with $V \gtrsim 21$ mag, the median R_{gal} is in the range where the rate of increase of r_h with increasing R_{gal} is significant (see panel (b) of Fig. 8). These relations are interpreted in terms of dynamical evolution processes in the next Section.

4.3. *Cluster Distribution in the 'Survival Diagram'*

The r_h versus cluster mass diagram is a useful tool to illustrate the 'survivability' of star clusters to various internal and external dissolution mechanisms (e.g. Fall & Rees 1977; Gnedin & Ostriker 1997; Georgiev et al. 2009). Fig. 10 shows the distribution of GCs in NGC 1316 with size measurements in this 'survival diagram', separately for blue and red GCs in panels (a) and (b). For comparison purposes, we include the same diagram for the Galactic GCs in panel (c). To convert luminosities of GCs in NGC 1316 into masses, we adopt M/L_V values of the SSP synthesis models of Bruzual & Charlot (2003), using a Chabrier (2003) initial mass function (IMF)[3]. We adopt age = 3 Gyr and [Z/H] = 0.0 for the red GCs (Goudfrooij et al. 2001a,b) and age = 13 Gyr and [Z/H] = −1.6 for the blue GCs, similar to the average properties of metal-poor GCs in our Galaxy (e.g. Harris 1996). For the Galactic GCs, half-light radii and cluster masses were taken from McLaughlin & van der Marel (2005) when available, and from Harris (1996) for the remainder. Symbol sizes scale with R_{gal}, as shown in the legend in the top right of the Figure.

Fig. 10 includes various lines that depict limits in the mass-radius plane imposed by various dynamical evolution mech-

---

[3] Use of the Maraston (2005) SSP models with a Kroupa (2001) IMF yields M/L_V values that are $\sim 5\%$ higher; applying the Salpeter (1955) IMF yields M/L_V values higher by $\sim 75\%$ relative to Chabrier or Kroupa IMFs.
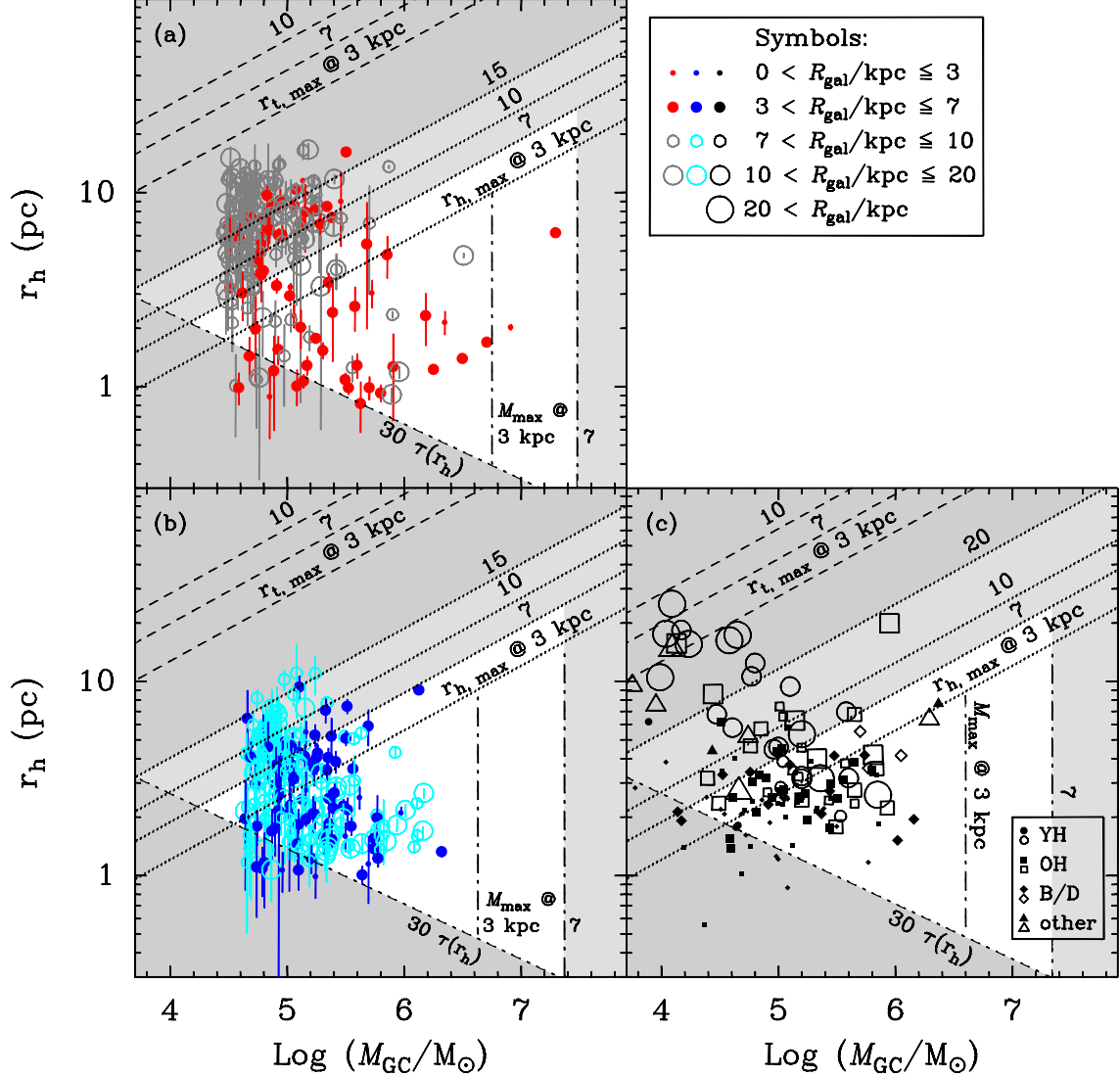
FIG. 10.— Half-light radius versus mass ('survival diagram') for GCs in NGC 1316 and our Galaxy. Symbol size indicates (projected) galactocentric radius as shown in the legend at the top right. Lines in each panel represent limits imposed by dynamical evolution effects at the galactocentric radii indicated above the line in question: Short-dashed lines indicate max. tidal radii, dotted lines indicate max. half-light radii, short-dashed-dotted lines indicate min. radii imposed by two-body relaxation, and long-dashed-dotted lines indicate max. masses imposed by dynamical friction. *Panel (a)*: Red GCs in NGC 1316 with $V \leq 25.3$. *Panel (b)*: Blue GCs in NGC 1316 with $V \leq 25.3$. *Panel (c)*: GCs in our Galaxy. Each subpopulation of Galactic GCs is represented by a different symbol, as shown in the legend. Abbreviations for Galactic GC subpopulations: OH = old halo; YH = young halo; B/D = bulge/disk. See discussion in Sect. 4.3.

anisms. To indicate limits imposed by the tidal field of NGC 1316, we calculate maximum tidal cluster radii $r_{t,max}$ by using the tidal limit for a satellite on a circular orbit:

$$r_{t,max} = \left(\frac{G\mathcal{M}_{cl}}{2V_{circ}^2}\right)^{1/3} R_{gal}^{2/3} \quad (2)$$

(e.g., Binney & Tremaine 1987; Baumgardt & Makino 2003) where V_{circ} is the circular velocity of the galaxy and R_{gal} is the galactocentric distance. For the latter, we multiply the observed (projected) galactocentric distances by a factor $2/\sqrt{3}$ to account for an assumed viewing angle of $60°$. We use $V_{circ} = 235 \text{ km s}^{-1}$ for NGC 1316; this represents the rotation velocity and velocity dispersion values added in quadrature using velocities of planetary nebulae and GCs (Arnaboldi et al. 1998; Goudfrooij et al. 2001b). $r_{t,max}$ is shown in Fig. 10 by short-dashed lines for three values of R_{gal}: 3, 7, and 10 kpc. To translate $r_{t,max}$ values to observed half-light radii $r_{h,max}$, we use the value of r_h/r_t for King models with $C_K = 30$, i.e.,

$r_h/r_t = 0.095^4$. Limits $r_{h,max}$ are drawn in Fig. 10 for $R_{gal} = 3$, 7, 10, and 15 kpc (for our Galaxy [i.e., panel c], the latter is 20 kpc), using dotted lines.

Dash-dotted lines represent limits imposed by cluster evaporation due to two-body relaxation:

$$r_{h,evap} = \left(\frac{t_{elapse}[\text{Myr}]}{N(t_{rel})}\right)^{2/3} \left(\frac{0.138}{\sqrt{G}m_\star \ln\left(\gamma\frac{\mathcal{M}_{cl}}{m_\star}\right)}\right)^{-2/3} \mathcal{M}_{cl}^{-1/3}$$

(3)

for clusters of *initial* mass $\mathcal{M}_{cl}$ that survived a time t_{elapse} after $N(t_{rel})$ initial relaxation times; $m_\star$ is the average stellar mass in a SSP of the appropriate age and metallicity, and $\gamma = 0.02$ is a correction constant taken from cluster simulations (Giersz & Heggie 1996). GCs with initial $r_h < r_{h,evap}$ will have dis-

---

[4] This choice was made for this figure because $C_K = 30$ provides the best fit for the majority of clusters in NGC 1316 and in our Galaxy. For reference, r_h/r_t values for $C_K = 15$ and 100 are 0.136 and 0.051, respectively.

solved after a time t_{elapse} of dynamical evolution (e.g. Fall & Zhang 2001). To facilitate the identification of red GCs in NGC 1316 that are likely to evaporate after 10 additional Gyr, we show $r_{\text{h,evap}}$ for $t_{\text{elapse}} = 10$ Gyr, $N(t_{\text{rel}}) = 30$ (see Gnedin & Ostriker 1997), and $m_\star = 0.55$ in panel (a) of Fig. 10. For panels (b) and (c) of Fig. 10 we use $t_{\text{elapse}} = 13$ Gyr, $N(t_{\text{rel}}) = 30$, and $m_\star = 0.49$, appropriate for 13 Gyr old populations with [Z/H] $= -1.6$. Note however that the GC masses plotted in Fig. 10 are *current* masses whereas $\mathcal{M}_{\text{cl}}$ in equation (3) refers to *initial* masses. I.e., one should take into account that GCs in panels (b) and (c) of Fig. 10 have already undergone some ~ 13 Gyr of dynamical evolution when comparing the cluster data with the lines that indicate limits in the mass-radius plane.

Maximum values for cluster mass imposed by dynamical friction in the galaxy potential ($\mathcal{M}_{\text{cl,max}}$) are estimated by using equation [7-26] of Binney & Tremaine (1987):

$$t_{\text{df}} = \frac{2.64 \times 10^{10}\,\text{yr}}{\ln\Lambda} \left(\frac{R_{\text{gal,i}}}{2\,\text{kpc}}\right)^2 \left(\frac{V_{\text{cl}}}{250\,\text{km s}^{-1}}\right) \left(\frac{10^5\,\text{M}_\odot}{\mathcal{M}_{\text{cl}}}\right), \quad (4)$$

where $\ln\Lambda$ is the Coulomb logarithm, $R_{\text{gal,i}}$ is the initial galactocentric distance, and V_{cl} is the velocity of the cluster with respect to the host galaxy. Values of the latter two parameters are estimated here by assuming $R_{\text{gal,i}} = R_{\text{gal}}$ and $V_{\text{cl}} = V_{\text{circ}}$. Values for $\mathcal{M}_{\text{cl,max}}$ are calculated by solving equation (4) for $\mathcal{M}_{\text{cl}}$ using $t_{\text{df}} = 10$ Gyr for the red GCs in NGC 1316, and $t_{\text{df}} = 13$ Gyr for the blue GCs in NGC 1316 and the Galactic GCs.

Overall, the distribution of blue GCs in NGC 1316 in the mass-radius plane is very similar to that of (metal-poor) halo GCs in our Galaxy. This is encouraging, since blue GCs in galaxies are commonly thought to represent the counterpart of halo GCs in our Galaxy. Note that the tail of the distribution of Galactic GCs towards low masses and large r_{h} values is not accessible in the NGC 1316 ACS data given its detection limit and limited radial coverage.

As to the distribution of red GCs in Fig. 10, it can be seen that the majority of the clusters are located in "healthy" regions for a 3-Gyr old population, taking their galactocentric radii into account. Furthermore, there are only a dozen or so GCs that are expected to evaporate completely in the next 10 Gyr due to two-body evaporation, and the effect of dynamical friction is expected to be negligible. However, several GCs in the top left region of panel (a) of Fig. 10 have r_{h} values that are larger than the $r_{\text{h,max}}$ value for their R_{gal}. This is illustrated in Fig. 11 which shows the same diagram as panel (a) of Fig. 10 except that different symbols now indicate the value of the ratio $r_{\text{h}}/r_{\text{h,max}}$. It seems likely that many of the red GCs with $r_{\text{h}}/r_{\text{h,max}} > 1$ will experience significant mass loss during ten additional Gyr of tidal shocking. The impact of dynamical evolution mechanisms on the distribution of red GCs in the 'survival diagram' and their mass function will be discussed in Section 5.

4.4. *Present-Day GC Mass Functions*

Observations of young star clusters in merging galaxies and young merger remnants show that the number of clusters per unit mass are well described by a power law, $dN/d\mathcal{M} \propto \mathcal{M}^\alpha$ with $\alpha \simeq -2$ (e.g., Fall et al. 2009). In the case of ancient GCs in massive "normal" galaxies with hundreds or even thousands of GCs, the mass function decreases more rapidly than a power law for masses larger than $\sim 3 \times 10^5$ M$_\odot$ (see Burkert

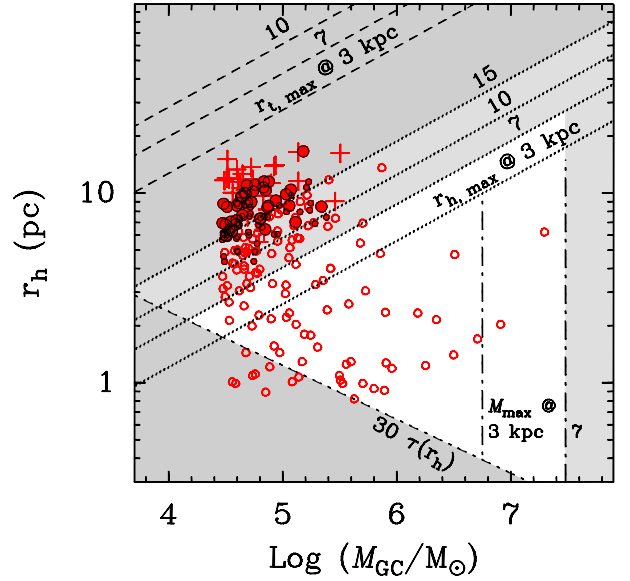FIG. 11.— Similar to panel (a) of Fig. 10, except that different symbols now indicate different values of the ratio $r_{\text{h}}/r_{\text{h,max}}$. Open circles indicate GCs with $r_{\text{h}}/r_{\text{h,max}} \leq 1.0$, small filled circles outlined in black indicate GCs with $1.0 < r_{\text{h}}/r_{\text{h,max}} \leq 1.5$, large filled circles outlined in black indicate GCs with $1.5 < r_{\text{h}}/r_{\text{h,max}} \leq 2.0$, and pluses indicate GCs with $r_{\text{h}}/r_{\text{h,max}} > 2.0$. See discussion in Sect. 4.3.

& Smith 2000). A function that provides an accurate description of the shape of mass functions of young clusters as well as the $\sim 50\%$ most massive GCs in ancient galaxies is the Schechter (1976) function, $dN/d\mathcal{M} \propto \mathcal{M}^\beta \exp(-\mathcal{M}/\mathcal{M}_c)$, with power-law component $\beta \simeq -2$ and exponential cutoff $\mathcal{M}_c$ above some large mass that might vary among galaxies (e.g., Burkert & Smith 2000; Gieles et al. 2006; Jordán et al. 2007, and references therein). This apparent connection between the GC mass function at high masses and that of young clusters and molecular clouds has been explained by theoretical models (McLaughlin & Pudritz 1996; Elmegreen & Efremov 1997). The main difference between the mass functions of ancient GCs and young clusters is the fact that the number of clusters per unit mass interval continues to rise like a power law towards the detection limit for young clusters, while it stays approximately constant among ancient GCs fainter than the classic peak magnitude of the GC luminosity function. The latter behavior is a signature of long-term dynamical evolution driven by two-body relaxation (Fall & Zhang 2001; Jordán et al. 2007).

Another signature of relaxation-driven dynamical evolution is that the evaporation time scale scales with cluster mass as $\tau_{\text{ev}} \propto \mathcal{M}_{\text{cl}} \rho_{\text{h}}^{-1/2}$, where $\rho_{\text{h}} = 3\mathcal{M}_{\text{cl}}/8\pi r_{\text{h}}^3$ is the mean density inside the cluster's half-mass radius. Under the common assumption that star clusters conserve their mean half-mass density while their dynamical evolution is dominated by evaporation (e.g., Vesperini 2000, 2001; Fall & Zhang 2001), this means that the peak mass $\mathcal{M}_{\text{p}}$ of the mass function of ancient cluster systems would scale with ρ_{h} as $\mathcal{M}_{\text{p}} \propto \rho_{\text{h}}^{1/2}$. McLaughlin & Fall (2008, hereafter MF08) found roughly this dependence of $\mathcal{M}_{\text{p}}$ on ρ_{h} among the old GCs in our Galaxy and argued that this presents evidence for a scenario that dynamical evolution shaped the mass function of ancient GC systems and that the dynamical evolution is dominated by two-body relaxation (see also Chandar et al. 2007, showing similar results for the Sombrero galaxy).

In the context of these recent studies, we reanalyze the mass functions of the blue and red GCs in NGC 1316 that have robust size measurements in the remainder of this Section. The completeness-corrected GC mass functions of the blue and red GCs with robust size measurements are shown in Figs. 12 and 13, respectively. The mass functions are shown in two bins of half-mass density ρ_h in the left-hand panels, and two bins of projected galactocentric radius R_{gal} in the right-hand panels. We plot the mass functions as $dN/d\log\mathcal{M} = (\mathcal{M}\ln 10)\,dN/d\mathcal{M}$ rather than $dN/d\mathcal{M}$ so as to create a shape similar to the familiar GC *luminosity* functions.

4.4.1. *Mass Function of Blue GCs*

The mass functions of the blue GCs in Fig. 12 show the familiar single-peaked "log-normal" shape of luminosity or mass functions of GCs in "normal" early-type galaxies, as expected for "ancient" GC systems (see, e.g., Jordán et al. 2007). Furthermore, Fig. 12 shows that the peak mass exhibits a clear dependence on ρ_h, whereas it depends much less strongly on R_{gal}. This is consistent with the situation for cluster mass functions in our Galaxy and the Sombrero galaxy (Chandar et al. 2007; MF08).

To enable a systematic comparison between the different peak cluster masses for different ranges of ρ_h and R_{gal}, we fit the data in Fig. 12 by a model mass function. For purposes of consistency with recent work on fitting mass functions of "old" star clusters (cf. above), we adopt a sum of so-called "evolved Schechter functions":

$$\frac{dN}{d\mathcal{M}} = \sum_i A_i \frac{1}{(\mathcal{M}+\Delta_i)^2} \exp\left(-\frac{\mathcal{M}+\Delta_i}{\mathcal{M}_c}\right) \quad (5)$$

(Jordán et al. 2007; Chandar et al. 2007; MF08) where $\Delta_i \equiv (\mu_{ev} t)_i \propto \sqrt{\rho_{h,i}}$ is the cumulative mass loss of cluster i, μ_{ev} is the rate of evaporative mass loss by two-body relaxation, t is the elapsed time (taken to be 13 Gyr in this case), A_i is a normalization constant for each cluster, $\mathcal{M}_c$ is the cutoff mass of the Schechter (1976) function, and the sum is over all clusters in the population. Following Chandar et al. (2007), we first fitted a model with a single term $\widetilde{\Delta}$ (the median value of Δ) in equation (5) to the mass functions for the full sample of 212 blue clusters to produce a "median" mass function which is depicted as the dashed curves in Fig. 12. After finding the best-fitting values for $\mathcal{M}_c$ and $\widetilde{\Delta}$, we determined the value of the normalization constant C_{ev} in $\widetilde{\Delta} = \widetilde{\mu_{ev}}\,t = C_{ev}\,\widetilde{\rho}_h^{1/2}$. Next, we fitted models for the two bins in ρ_h and the two bins in R_{gal} using separate terms for each cluster in equation (5), using the values for $\mathcal{M}_c$ and C_{ev} derived above. These models are shown by solid curves in Fig. 12. The peak mass $\mathcal{M}_p$ corresponding to the turnover magnitude of GC luminosity functions is found from the values of $\widetilde{\Delta}$ and $\mathcal{M}_c$ by solving

$$\partial\left(\log\left(\frac{dN}{d\log\mathcal{M}}\right)\right)\Big/\partial(\log\mathcal{M}) = 0 \quad (6)$$

for $\mathcal{M}$, to which the solution is

$$\mathcal{M}_p = \frac{-(\widetilde{\Delta}+\mathcal{M}_c)+\sqrt{(\widetilde{\Delta}+\mathcal{M}_c)^2+4\widetilde{\Delta}\mathcal{M}_c}}{2}. \quad (7)$$

Resulting values for $\mathcal{M}_p$, $\widetilde{\Delta}$ and $\widetilde{\rho}_h$ for each bin in ρ_h and R_{gal} are listed in Table 2. It turns out that $\widetilde{\Delta}$ scales with $\widetilde{\rho}_h$ as $\widetilde{\Delta} \propto \widetilde{\rho}_h^{\beta}$ with $\beta = 0.44 \pm 0.10$. This is consistent with the

predicted scaling $\Delta \propto \rho_h^{1/2}$ for two-body relaxation, given the exponential cutoff of the Schechter function at $\mathcal{M}_c$.

4.4.2. *Mass Function of Red GCs*

Fig. 13 shows that the mass function of the red GCs in NGC 1316 has much in common with the power-law mass functions of young massive clusters. In fact, the mass function of the full sample of 212 red GCs is very well fit by a power law $dN/d\mathcal{M} \propto \mathcal{M}^{\alpha}$ with $\alpha = -1.88 \pm 0.04$, consistent with those found in younger merger remnants and starburst galaxies (e.g., Meurer et al. 1995; Fall et al. 2009). However, splitting the cluster system into two bins of ρ_h and two bins of R_{gal} reveals more information about the dynamical state of the red GC system. Performing power-law fits to the mass function of the four cluster subsamples shows that the value of α differs systematically between the subsamples in the sense that the slope is steepest for the lowest-density clusters and flattest for the highest-density clusters, with the two bins in R_{gal} showing intermediate values of α. This suggests that evaporation by two-body relaxation has already had a measurable impact on the clusters' dynamical evolution. The apparent flattening of the mass function at $\log(\mathcal{M}_{cl}/M_\odot) \lesssim 5.0$ in the high-density subsample (i.e., panel [b] of Fig. 13) indicates this as well. To check whether this flattening is at all consistent with the expected shape of the cluster mass function at an age of 3 Gyr due to two-body relaxation, we adopt the mass density-dependent mass loss rate μ_{ev} found above for the full system of *blue* GCs in NGC 1316, i.e.,

$$\mu_{ev} = 875\left(\frac{\rho_h}{M_\odot\,pc^{-3}}\right)^{1/2} M_\odot\,Gyr^{-1} \quad (8)$$

(see values of $\widetilde{\Delta}$ and $\widetilde{\rho}_h$ for all blue GCs in Table 2). Inserting equation (8) into equation (5) and assuming $t = 3$ Gyr for the red clusters, we fit equation (5) to the two bins in ρ_h and the two bins in R_{gal}, using separate terms for each individual cluster as done in the previous section. Resulting values for $\mathcal{M}_p$ for each subsample are listed in Table 2, and the resulting mass function fits are shown in Fig. 13 as dashed curves. Note that the fitted mass functions are consistent with the data, including the apparent flattening of the mass function at $\log(\mathcal{M}_{cl}/M_\odot) \lesssim 5.0$ in the high-density subsample.

This result is consistent with our earlier claims in Goudfrooij et al. (2004), even though the latter study used incorrect aperture corrections for the large red clusters, which are mainly located in the outer regions. Furthermore, we can now quantify that the flattening of the mass function is stronger for clusters with high mass density than those with smaller galactocentric radii, as expected if two-body relaxation dominated the dynamical evolution (but see Section 5.2).

5. DYNAMICAL EVOLUTION OF THE INTERMEDIATE-AGE CLUSTER POPULATION

As mentioned in the Introduction, the population of red clusters in the 3-Gyr-old merger remnant NGC 1316 provides an important opportunity to test whether and how the power-law LFs seen in young merger remnant galaxies may evolve into the ubiquitous bell-shaped LFs of ancient GCs in "normal" galaxies. This topic is addressed in this Section by applying dynamical evolution model calculations from the recent literature to the observed current properties of the red clusters in NGC 1316. To compare the results with ancient GCs in "normal" galaxies, we let the red clusters evolve dynamically for another 10 Gyr. Mass loss by stellar evolution is
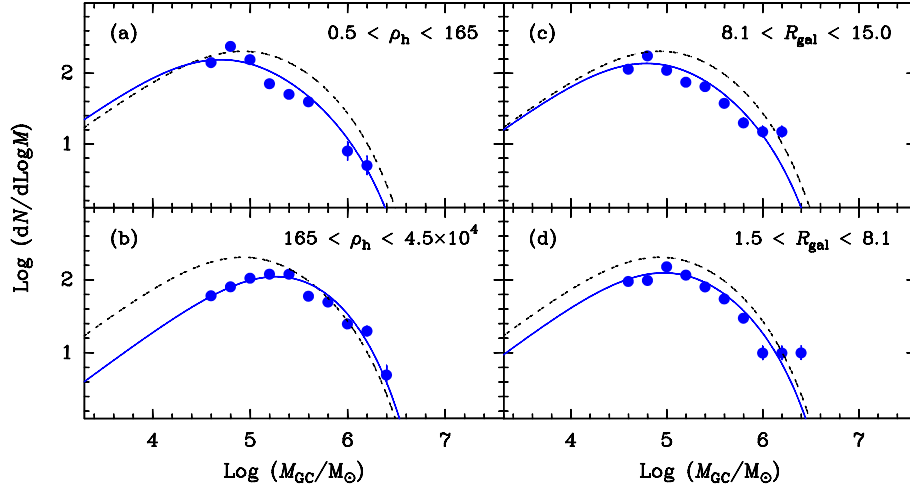
FIG. 12.— Mass functions of blue clusters in NGC 1316 with robust size measurements. Panels (a) and (b) show data for two ranges of half-mass density $\rho_{\rm h}$ in units of $M_\odot$ pc^{-3}, as indicated in the legend. Panels (c) and (d) show data for two ranges of projected galactocentric distance $R_{\rm gal}$ in kpc, as indicated in the legend. The solid curves were computed from equation (5) by summing over mass-loss terms for all individual clusters within the bins of $\rho_{\rm h}$ or $R_{\rm gal}$ mentioned in each panel. For comparison purposes, the dashed curve in each panel was computed from equation (5) with a single term using the median value of $\rho_{\rm h}$ for the full sample of 212 blue clusters.
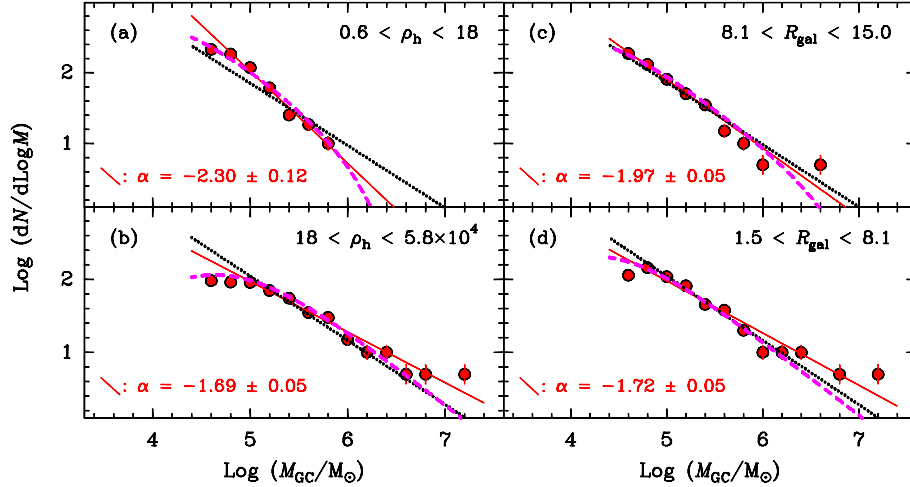

FIG. 13.— Mass functions of red clusters in NGC 1316 with robust size measurements. Panels (a) and (b) show data for two ranges of half-mass density $\rho_{\rm h}$ in units of $M_\odot$ pc^{-3}, as indicated in the top right. Panels (c) and (d) show data for two ranges of projected galactocentric distance $R_{\rm gal}$ in kpc, as indicated in the top right. The (red) solid curves represent power-law fits to the mass functions for $\mathcal{M}_{\rm GC} > 10^5$ $M_\odot$. The value of α in $dN/d\mathcal{M} \propto \mathcal{M}^\alpha$ is stated at the lower left of each panel. For comparison purposes, the (black) dotted curve in each panel represents a power-law fit to the mass function of the full sample of 212 red clusters, for which $\alpha = -1.88 \pm 0.04$. The dotted curve was normalized to the solid curve at log $(\mathcal{M}_{\rm GC}/M_\odot) = 5.4$ in each panel to facilitate the comparison. Finally, the (magenta) dashed curves represent fits of equation (5) to the data by summing over mass-loss terms for all individual clusters in the samples represented in each panel. See Sect. 4.4.2 for details.

also taken into account, using the BC03 SSP models at solar metallicity which yield a mass loss of 9% between ages of 3 and 13 Gyr.

5.1. *Evaporation by Two-Body Relaxation*

We use two independent models to evaluate the effect of evaporation by two-body relaxation to the red GCs in NGC 1316 over the next 10 Gyr.

(i) The McLaughlin & Fall (2008) model. We first use the aforementioned model of MF08 who argue that the change in shape of the globular cluster mass function (GCMF) from young to old systems is due mainly to evaporation by two-body relaxation (see also Fall & Zhang 2001). Driven by their finding that the dependence of the peak mass $\mathcal{M}_{\rm p}$ of the Galactic GCMF on half-mass density is approximately $\mathcal{M}_{\rm p} \propto \rho_{\rm h}^{1/2}$, as predicted for evaporation by internal two-body relaxation, they suggest that evaporation by two-body relax-

ation is dominated by effects internal to the clusters and ignore the influence of the tidal field of the galaxy. We use equation (8) derived above for the blue GCs in NGC 1316 to estimate evaporation-driven mass loss for the red GCs according to the MF08 model. The resulting distribution of the surviving red GCs at an age of 13 Gyr in the mass-radius plane is shown in panel (b) of Fig. 14.

(ii) The Baumgardt & Makino (2003) model. Baumgardt & Makino (2003, hereafter BM03) performed extensive N-body simulations of star clusters, taking a (static) Galactic tidal field into account. Similar to MF08, they assume that GCs fill their Roche lobe in the tidal field. Adopting a King model with $W_0 = 7$ (i.e., $C_K \simeq 30$), we use their equation (7) to calculate dissolution times $t_{\rm diss}$ in Gyr for each red GC. In case $t_{\rm diss} > 10$ Gyr, remaining GC masses at an age of 13 Gyr were approximated using $\mathcal{M}_{\rm cl}(13\,{\rm Gyr}) = 0.91\,\mathcal{M}_{\rm cl,0}(1 - 10/t_{\rm diss})$ where $\mathcal{M}_{\rm cl,0}$ is the current cluster mass (see BM03). We employ
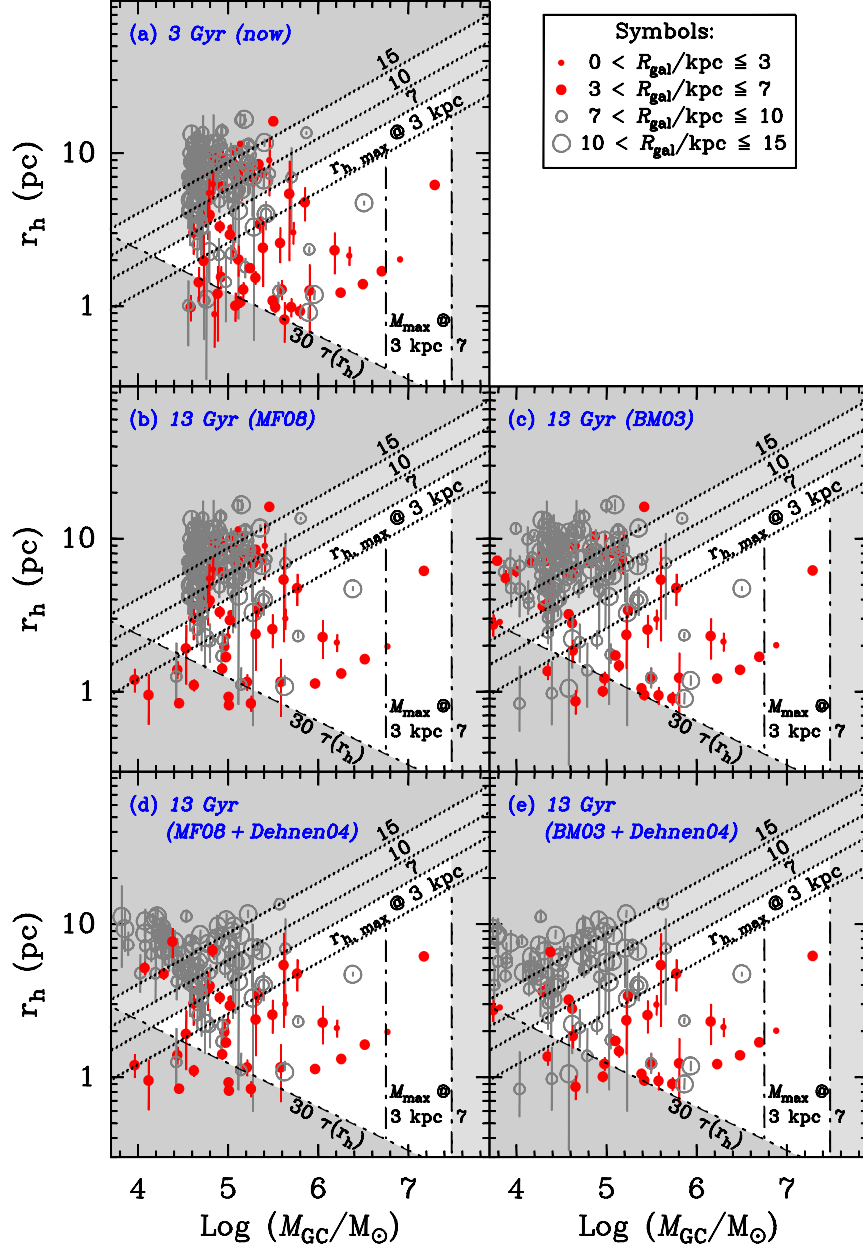
FIG. 14.— Survival diagram for the red clusters in NGC 1316 as function of time using dynamical evolution calculations described in §§ 5.1 and 5.2. Panel (a) shows the same data as Fig. 10a for reference. Panel (b) shows the surviving clusters at an age of 13 Gyr after applying mass loss due to two-body relaxation according to the prescriptions of MF08. Panel (c) is similar to panel (b), except that mass loss due to two-body relaxation has been applied according to the prescriptions of BM03. Panels (d) and (e) are similar to panels (b) and (c), respectively, except that mass loss due to tidal shocks according to prescriptions of Dehnen et al. (2004) has also been applied. Symbols are shown in the legend in the upper right.

circular GC orbits for this exercise, recognizing that dissolution times vary with orbit eccentricity ϵ approximately as $t_{\rm diss}(\epsilon) = (1-\epsilon)\,t_{\rm diss}(0)$ (see BM03). Panel (c) of Fig. 14 shows the distribution of the surviving red GCs at an age of 13 Gyr in the mass-radius plane according to the BM03 model.

Comparing panels (b) and (c) of Fig. 14, one can see that the MF08 model yields higher mass loss for compact low-mass GCs while the BM03 model yields higher mass loss for larger GCs at a given initial mass. However, it is also clear that both models predict little mass loss for GCs with $\mathcal{M}_{\rm cl,0} \lesssim 10^5$ M$_\odot$ and $r_{\rm h} \gtrsim 7$ pc, especially the MF08 model. Note that such diffuse, low-mass clusters are quite common in NGC 1316 even though they are rare in "normal" elliptical galaxies. This is further discussed below.

5.2. Diffuse Red Clusters and the Influence of Tidal Shocks

While diffuse, low-mass, red clusters such as those seen in NGC 1316 have hitherto not been identified in nearby "normal" elliptical galaxies, they are known to exist in about a dozen nearby lenticular (S0) galaxies (such clusters are sometimes called "faint fuzzies"; Larsen & Brodie 2000; Brodie & Larsen 2002; Peng et al. 2006b). Studies of the lenticular galaxies that host such clusters commonly found various signatures of past interactions with neighboring galaxies (Brodie & Larsen 2002; Hwang & Lee 2006, and references therein). The presence of several such clusters in the intermediate-age merger remnant NGC 1316 seems relevant in this context, also because its body's dynamical v/σ ratio is consistent with an isotropic rotator (Arnaboldi et al. 1998), which is a typical

signature of lenticular galaxies (e.g., Bender 1988).

The population of such "diffuse" clusters in lenticular galaxies is typically fainter than the turnover of the GC luminosity function (of "normal" galaxies, i.e., $M_V \simeq -7.4$, equivalent to $\mathcal{M}_{cl} \simeq 1.5 \times 10^5$ M$_\odot$), with colors similar to the brighter "red" clusters (Brodie & Larsen 2002; Peng et al. 2006b). The situation for diffuse clusters in NGC 1316 is very similar, except that the mass range of the latter seem to extend to masses higher by a factor of $2-5$ (viz. Fig. 11), which may in turn be due to such clusters having been exposed to dynamical evolution processes for a significantly shorter time in NGC 1316 than in "normal" galaxies. This raises the question: could the diffuse red clusters seen in the merger remnant NGC 1316 represent the precursors of their counterparts seen in "normal" lenticular galaxies? If so, what would their masses be at an age of 13 Gyr?

As discussed in the previous Section, evaporation by internal two-body relaxation is very ineffective for diffuse clusters with such low densities. In the absence of dynamical processes with higher mass loss efficacy for such clusters, the prevalence of such clusters in NGC 1316 would therefore seem at odds with the significantly lower frequency of such clusters in "normal" lenticular galaxies. However, a key feature of such clusters in NGC 1316 is that they typically have $r_h > r_{h,max}$, i.e., their sizes are larger than the upper limit imposed by the tidal field of the host galaxy at their R_{gal} (see Sect. 4.3 and Fig. 11). This indicates that a significant fraction of the stars in such clusters is located outside the Roche lobe of the cluster, i.e., the outer limit of the "bound" part of such clusters that is in equilibrium with the tidal field of the host galaxy. Disruption of these diffuse clusters by tidal shocks is therefore expected to be significantly faster than for clusters that are tidally limited, i.e., clusters that do not extend beyond their Roche lobe. To our knowledge, the N-body simulation study of Dehnen et al. (2004) is the only one to date that addresses the dynamical evolution of this type of "supertidal", low-density star cluster by galactic tides in detail. Dehnen et al. model the disruption of the diffuse Galactic cluster Palomar 5, for which $r_h \simeq 20$ pc and $r_h/r_{h,max} \approx 2$ (see also Odenkirchen et al. 2003), similar to many diffuse clusters in NGC 1316. The simulations of Dehnen et al. (2004) suggest that clusters with $r_h/r_{h,max} > 1$ that move along eccentric orbits never become tidally limited[5]. This would mean that their dynamical evolution would be mainly driven by tidal shocks rather than evaporation by two-body relaxation. For the case of Palomar 5 which has a current mass of $\sim 5 \times 10^3$ M$_\odot$, Dehnen et al. (2004) find that a cluster with an orbit-averaged mass loss $\dot{\mathcal{M}}_{cl} = 5 \times 10^3$ M$_\odot$ Gyr^{-1} yields the best fit. For an assumed age of 13 Gyr for Palomar 5, this implies a mass of 5.5×10^4 M$_\odot$ at an age of 3 Gyr assuming a constant Galactic tidal field strength. Note that this mass is just above the low-mass end of the diffuse clusters in NGC 1316 (with reliable size measurements). Using the values of $\dot{\mathcal{M}}_{cl}/\mathcal{M}_{cl,0}$ as function of $r_h/r_{h,max}$ and W_0 from the simulations of Dehnen et al. (2004) (using polynomial interpolation), we estimate masses at an age of 13 Gyr for the clusters in NGC 1316 with $r_h/r_{h,max} > 1$ for the case of $W_0 = 4.2$. To do so, the

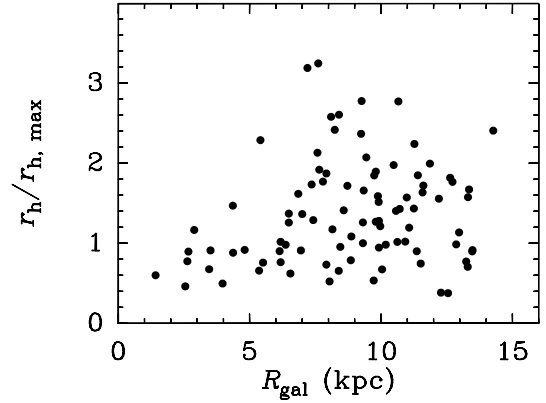FIG. 15.— $r_h/r_{h,max}$ as function of galactocentric distance for red clusters with $4.6 < \log(\mathcal{M}_{cl}/M_\odot) < 4.8$. Note the scarcity of "supertidal" clusters with $r_h/r_{h,max} \gtrsim 2$ at $R_{gal} \lesssim 5$ kpc.

values of $\dot{\mathcal{M}}_{cl}/\mathcal{M}_{cl,0}$ from Dehnen et al. were scaled for a given cluster by considering that the mass loss timescale due to tidal shocks τ_{sh} scales as $\tau_{sh} \propto P_{cl}$ (e.g., Gnedin et al. 1999). Here P_{cl} is the period of the cluster's orbit, estimated as $P_{cl} \approx 2\pi R_{gal}^{3/2}(G\mathcal{M}_{<R_{gal}})^{-1/2} \approx 2\pi R_{gal}(V_{circ}^2/3)^{-1/2}$, where $\mathcal{M}_{<R_{gal}}$ is the mass of NGC 1316 inside the galactocentric distance of the cluster in question. In this context we assume $R_{gal} = 16.4$ kpc for Palomar 5, which is the equivalent radius of its eccentric orbit (Odenkirchen et al. 2003). The results are shown in panels (d) and (e) of Fig. 14.

Note that the application of the Dehnen et al. (2004) calculations indeed predicts that many of the diffuse red clusters in NGC 1316 will end up in the area within the survival diagram known to be occupied by diffuse low-mass clusters in our Galaxy (several 'Palomar'-type clusters; see panel (c) of Fig. 10). Hence, this yields a low-mass tail to the cluster mass function that is lacking when only applying cluster disruption due to two-body relaxation (especially for the MF08 model).

An interesting side consequence of the results of the Dehnen et al. (2004) simulations is that they would explain why the supertidal clusters with masses close to the low-mass cutoff implied by the constraint of avoiding biases related to varying incompleteness (i.e., $V < 25.3$ mag) are only found in the outer regions of NGC 1316. To illustrate this, we plot R_{gal} versus the ratio $r_h/r_{h,max}$ in Figure 15 for all red clusters with $25.3 > V > 24.8$ mag, corresponding to $4.6 < \log(\mathcal{M}_{cl}/M_\odot) < 4.8$. This plot shows clearly that diffuse clusters with $r_h/r_{h,max} \gtrsim 2$ are only found at $R_{gal} \gtrsim 5$ kpc. Taking the median value of R_{gal} for clusters with $4.6 < \log(\mathcal{M}_{cl}/M_\odot) < 4.8$ and $1.8 < r_h/r_{h,max} < 2.2$ as a proxy ($\widetilde{R_{gal}} = 9.0$ kpc), we obtain a typical value of $\dot{\mathcal{M}}_{cl}/\mathcal{M}_{cl,0} = -0.12$ Gyr^{-1} from the Dehnen et al. simulations for the case of $W_0 = 4.2$ and $r_h/r_{h,max} = 2.0$. For a 3-Gyr-old cluster with $\log(\mathcal{M}_{cl}/M_\odot) = 4.80$, we then obtain $\log(\mathcal{M}_{cl,0}/M_\odot) = 5.06$ at an age of $\approx 10^8$ yr (i.e., after the bulk of mass loss due to stellar evolution has already occurred). Figure 16a shows $\mathcal{M}_{cl}$ versus time for such a cluster for six values of R_{gal} assuming $\dot{\mathcal{M}}_{cl}/\mathcal{M}_{cl,0} = -0.12$ Gyr^{-1} at $R_{gal} = 9$ kpc. The low-mass cutoff of $\log(\mathcal{M}_{cl}/M_\odot) = 4.6$ is indicated by a dotted horizontal line. Note that the Dehnen et al. simulations predict that such a cluster would only remain in a magnitude-limited sample with $V < 25.3$ mag at an age of 3 Gyr for $R_{gal} \gtrsim 5$ kpc, consistent with what we see. This suggests that *the absence of such low-mass "supertidal" clusters in the inner regions of NGC 1316 is caused by tidal shocking* rather than due to

---

[5] This is unlike more "typical" surviving GCs, which feature higher ρ_h and experience tidal shocks on time scales that are long relative to their dynamical time. For such clusters, tidal shocks are thought to cause significant mass loss only during their first few galactic orbits (Gnedin et al. 1999; Fall & Zhang 2001) or during galaxy interactions (Kruijssen et al. 2011). At an assumed age of 3 Gyr, the red clusters in NGC 1316 already went through this era.
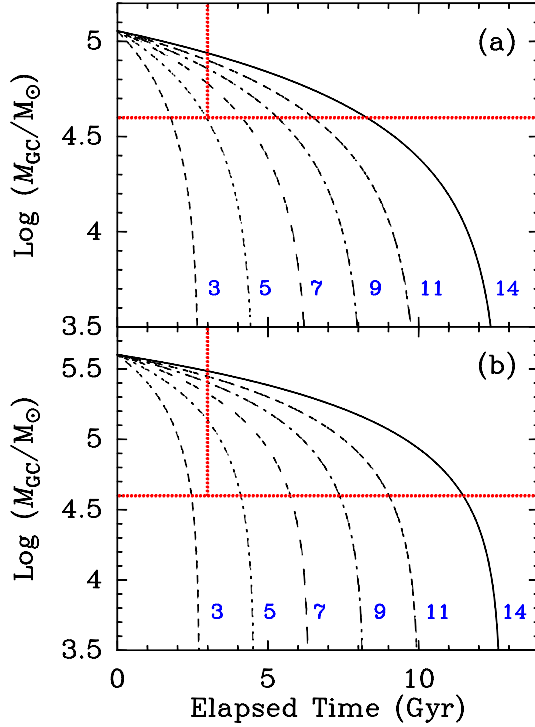
FIG. 16.— *Panel (a):* Dynamical evolution due to tidal shocking according to simulations of Dehnen et al. (2004) for a cluster with $r_h/r_{h,max} = 2$ and $\log(\mathcal{M}_{cl,0}/M_\odot) = 5.06$ for six values of galactocentric distance R_{gal} in NGC 1316. The values of R_{gal} in kpc are indicated near the bottom of the plot, to the right of their respective associated curves. The horizontal dotted line indicates the low-mass cutoff of the nominal cluster sample. The vertical dotted line indicates an elapsed time of 3 Gyr, the assumed age of the red clusters in NGC 1316. *Panel (b):* Similar to panel (a), but for $\log(\mathcal{M}_{cl,0}/M_\odot) = 5.60$. See discussion in Sect. 5.2.

(e.g.) completeness-related issues. Incidently, this could also be the reason why Larsen & Brodie (2000) find a deficit of "faint fuzzies" in the central regions of the lenticular galaxy NGC 1023. For comparison purposes, Figure 16b shows the same as Figure 16a but for $\log(\mathcal{M}_{cl,0}/M_\odot) = 5.6$, which yields a cluster with a mass at age = 3 Gyr that is similar to the maximum mass attained by diffuse red clusters in NGC 1316. Note that such clusters are predicted to stay detectable in the outer regions of NGC 1316 for 10-12 Gyr, which is consistent with them having been detected in the outskirts of some nearby "normal" S0 galaxies.

We note that the simulations of Dehnen et al. (2004) only covered a limited parameter space in $\mathcal{M}_{cl}$, $r_h/r_{h,max}$ and W_0, and they used a gravitational potential model for our Galaxy. Hence, these results should be used with caution in a quantitative sense. Unfortunately, other N-body simulations of tidal stripping of clusters that extend beyond their Roche lobe are still lacking in the literature to our knowledge. Given the results shown here, it seems quite useful to perform such simulations for clusters with a range of properties encompassing those found for the diffuse red clusters in NGC 1316 as well as a more appropriate galactic potential (e.g., using a more massive bulge component). Such calculations would yield relevant (more quantitative) insights into the important question whether these clusters may indeed evolve into the "extended clusters" or "faint fuzzies" found in older lenticular galaxies which often show lingering evidence of interactions with other galaxies (e.g., nearby neighbors, see Brodie & Larsen 2002; Peng et al. 2006b). The nature of diffuse red clusters is further discussed in Sect. 6.3.

5.3. *Resulting Mass Functions of Red GCs*

In the context of building mass functions for the red clusters at an age of 13 Gyr from the dynamical evolution calculations mentioned above, we recall that so far, we only considered clusters with $V \leq 25.3$ mag in order to avoid biases related to varying incompleteness for fainter clusters (see Section 4.1). However, it is likely that the assumed magnitude limit has an impact on the resulting mass function at low masses. To evaluate this impact, we build mass functions for two magnitude limits: $V \leq 25.3$ mag (as before) and $V \leq 25.8$ mag. For reference, the completeness fraction in the latter (fainter) cluster sample is $\gtrsim 0.20$ as opposed to $\gtrsim 0.46$, and the minimum S/N returned by the ISHAPE fits is ~ 22 as opposed to ~ 50.

The completeness-corrected cluster mass functions resulting from the calculations mentioned above are shown in Figs. 17 and 18 (using two-body relaxation prescriptions from MF08 and BM03, respectively). Mass functions are again shown for two bins of ρ_h in the left-hand panels, and two bins of R_{gal} in the right-hand panels. The curves drawn in Figs. 17 and 18 represent fits of equation (5) to the cluster masses evolved to an age of 13 Gyr using cluster disruption due to both two-body relaxation and tidal shocks (i.e., the filled symbols), performed in a manner identical to that described in Section 4.4 and shown in Fig. 12. Resulting values for $\mathcal{M}_p$, Δ and $\widetilde{\rho}_h$ for each bin in ρ_h and R_{gal} are again listed in Table 2.

Figs. 17 and 18 show several items of interest. First of all, the estimated mass functions for an age of 13 Gyr appear roughly similar to the familiar shape of luminosity or mass functions of GCs in "normal" early-type galaxies. Secondly, Figs. 17 and 18 both show that $\mathcal{M}_p$ exhibits a clear dependence on ρ_h, whereas it depends less strongly on R_{gal}. This statement is reinforced by the fact that the dependence on ρ_h is stronger for the sample with $V \leq 25.8$ mag than that with $V \leq 25.3$ mag. Quantitatively, the mass function fits to the red clusters with $V \leq 25.8$ mag imply that $\widetilde{\Delta} \propto \widetilde{\rho}_h^{\beta}$ with $\beta = 0.41 \pm 0.10$ when applying the MF08 prescriptions for two-body relaxation, and $\beta = 0.44 \pm 0.10$ when applying the BM03 prescriptions. This is again consistent with the situation for cluster mass functions in our Galaxy and the Sombrero galaxy (Chandar et al. 2007; MF08) as well as with our findings for the "blue" metal-poor GCs in NGC 1316 (see Sect. 4.4 and Fig. 12), and hence with the notion that dynamical evolution by two-body relaxation is an important mechanism in shaping cluster mass functions after the early era of rapid mass loss by stellar evolution and gas expulsion (e.g., MF08). However, the shapes of the estimated mass functions are significantly better matched to those of the overplotted model fits (evolved Schechter functions) for the calculations that take into account disruption of the diffuse "supertidal" clusters due to tidal shocks than those that do not. This effect is illustrated most clearly in Fig. 17a where the calculations that use the MF08 model of mass loss by two-body relaxation (i.e., the open squares) are poorly fit by evolved Schechter functions (Eq. 5) at masses $\lesssim 10^5$ $M_\odot$. This suggests that the observed functional dependence of $\mathcal{M}_p$ on ρ_h among ancient cluster systems is *not necessarily due to evaporation by two-body relaxation alone*. Our analysis suggests that it may be due in part to disruption of very low-density "supertidal" clusters by tidal shocks. The reason why the effect of disruption of supertidal clusters by tidal shocks can "masquerade" as that of two-body relaxation in mass function plots is that both mechanisms are characterized by mass loss rates that are highly linear with time (see Dehnen et al. 2004; Jordán et al.
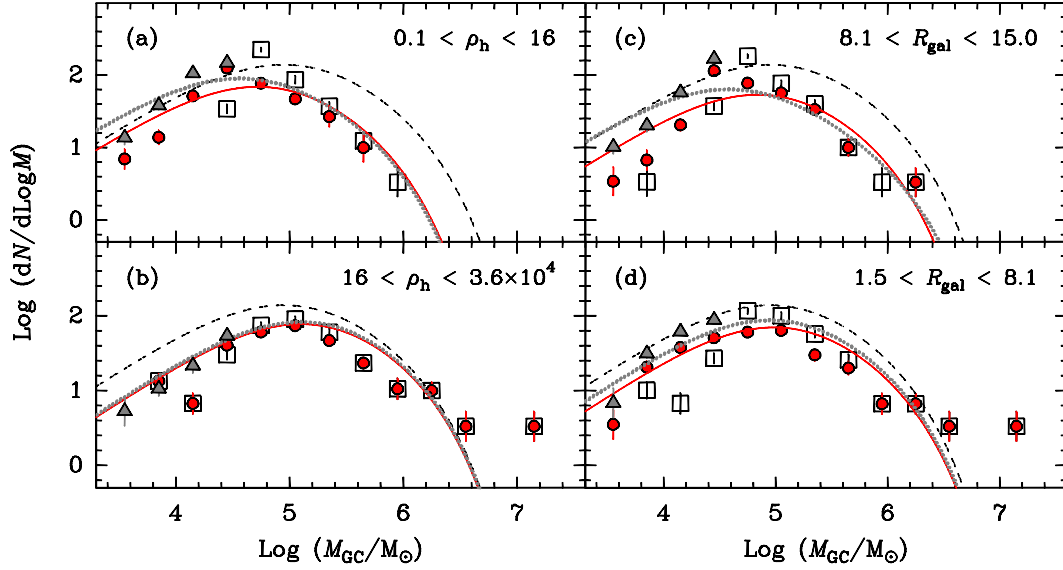
FIG. 17.— Predicted mass functions of red clusters in NGC 1316 shown in panel (c) of Fig. 14 at an age of 13 Gyr, using MF08 prescriptions for mass loss by two-body relaxation. Panels (a) and (b) show data for two ranges of half-mass density ρ_h in units of $M_\odot$ pc^{-3}, as indicated in the legend. Panels (c) and (d) show data for two ranges of projected galactocentric distance R_{gal} in kpc as indicated in the legend. Open squares represent results using *only* mass loss due to two-body relaxation, while filled (red) circles represent results that take into account additional mass loss due to tidal shocking according to simulations of Dehnen et al. (2004). The solid (red) curves represent fits of equation (5) to the filled circles by summing over mass-loss terms for all individual clusters within the bins of ρ_h or R_{gal} mentioned in each panel. For comparison purposes, the dashed (black) curve in each panel was computed from equation (5) with a single term using the median value of ρ_h for the full sample of 192 surviving red clusters. Finally, the filled (grey) triangles and the dotted lines depict the same results as the filled circles and the solid lines, respectively, but now for red clusters with $V < 25.8$ instead of $V < 25.3$. See discussion in Section 5.3.
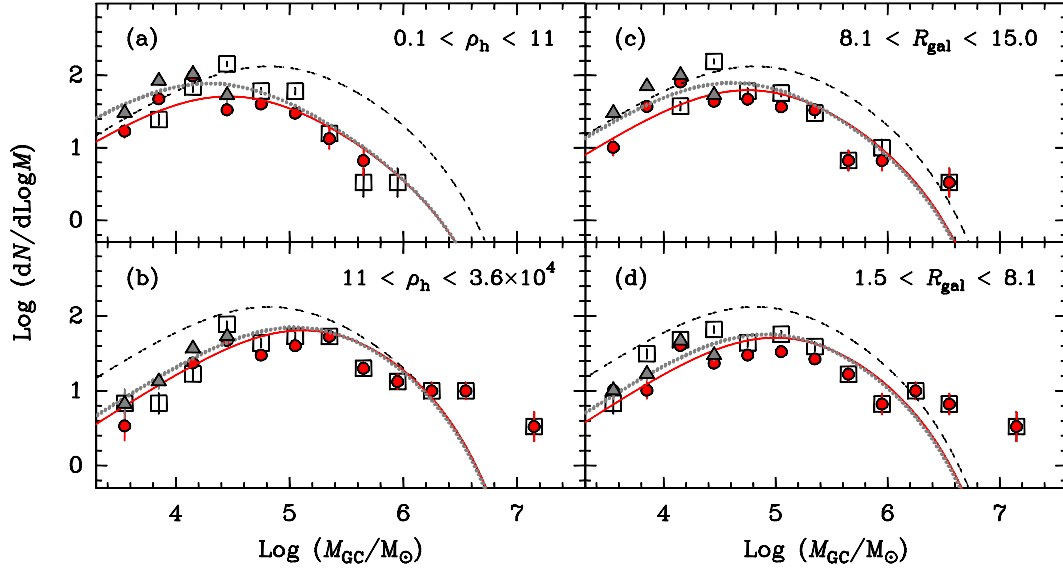

FIG. 18.— Same as Fig. 17, but now for the red clusters shown in panels (c) and (e) of Fig. 14, i.e., using the BM03 prescriptions for mass loss by two-body relaxation.

2007).

Finally, we comment on the impact of the possibility that a small fraction of the fainter red GCs in NGC 1316 are in fact "old" ($\simeq 13$ Gyr rather than 3 Gyr old; cf. Section 2) on the mass functions shown in Figures 17 and 18. Since ancient red GCs in "normal" early-type galaxies typically have radii of $1-4$ pc (e.g., Jordán et al. 2005; Paolillo et al. 2011), Figure 14 shows that the impact of a small fraction of red GCs being old is predicted to be insignificant. Specifically, the dynamical evolution from 3 Gyr to 10 Gyr performed in this Section would have moved of order $7-10$ of the red GCs with $1 \lesssim r_h \lesssim 4$ pc incorrectly to lower mass bins, but the mass function at those lower masses is entirely dominated by

the GCs with $r_h \gtrsim 5$ pc since the tidal shocks in the Dehnen et al. (2004) model are only effective for the latter GCs.

6. SUMMARY AND DISCUSSION

Using *HST/ACS* images, we have conducted size measurements of GCs in the giant ~ 3-Gyr-old merger remnant galaxy NGC 1316 to obtain insights on the dynamical status of its "blue" (metal-poor) and "red" (metal-rich) GC subpopulations. Using simulations and calculations of cluster disruption from the recent literature, we make predictions on the effect of 10 Gyr of dynamical evolution of the red GCs which are assumed to have an age of 3 Gyr based on earlier work. These results are used in the context of evaluating the scenario that

the "red" GCs in "normal" giant early-type galaxies (along with their bulge component) were formed in a way similar to that observed in gas-rich galaxy mergers today.

6.1. *Dynamical Status of the Blue GCs*

For the blue GCs, we find that their properties are consistent with those typically found for blue GCs in "normal" giant early-type galaxies. The GC mass function (MF) is consistent with an lognormal distribution, similar to the MF of ancient GCs in normal giant galaxies. The peak mass $\mathcal{M}_p$ of the MF of the blue GCs increases with half-mass density ρ_h as $\mathcal{M}_p \propto \rho_h^{0.44\pm0.10}$ whereas it stays approximately constant with R_{gal}. As found recently for ancient GCs in the Milky Way and the Sombrero galaxy (Chandar et al. 2007; McLaughlin & Fall 2008), the mass functions of the blue GCs are consistent with a simple scenario in which the clusters formed with a Schechter initial mass function and evolved subsequently by disruption driven mainly by internal two-body relaxation (but see the last paragraph of Section 6.2 below).

6.2. *Dynamical Status of the Red GCs*

For the intermediate-age metal-rich (red) GCs, we find that the faint end of the previously reported luminosity function of the clusters outside a galactocentric radius of 9 kpc (which showed a power-law, Goudfrooij et al. 2004) is due to those low-mass clusters having half-light radii large enough for disruption by two-body relaxation to be ineffective. This is especially the case when considering the MF08 prescriptions for mass loss due to two-body relaxation. Moreover, we find that the radii of many of these diffuse red GCs are larger than the theoretical maximum value imposed by the tidal field of NGC 1316 at their R_{gal}. We therefore suggest that the diffuse "supertidal" clusters in NGC 1316 lose a large fraction of their mass due to tidal shocks in a way similar to that described by the simulations of Dehnen et al. (2004) which were performed to understand the properties of the extended cluster Palomar 5 in our Galaxy. Application and scaling of the Dehnen et al. simulations to these "supertidal" clusters in NGC 1316 in addition to the application of cluster disruption by two-body relaxation yields several findings relevant to the nature of the red GCs:

1. Clusters larger than twice the maximum radius imposed by the tidal field of NGC 1316 with $\log(\mathcal{M}_{cl}/M_\odot) \lesssim 5.1$ at an age of $\approx 10^8$ yr (i.e., after the era of strong mass loss due to stellar evolution) would not survive to an age of 3 Gyr in NGC 1316 if located within $R_{gal} \lesssim 5$ kpc, which is consistent with the observations. Note that such clusters with $\log(\mathcal{M}_{cl}/M_\odot) \gtrsim 4.6$ *would* be detectable there according to our completeness calculations.

2. Another 10 Gyr of simulated dynamical evolution of the red GCs yields a MF whose shape is similar to the lognormal shape of MFs of ancient GCs in normal galaxies *throughout the range of galactocentric distances covered by the observations*. The peak mass $\mathcal{M}_p$ of the simulated MF of the red GCs at an age of 13 Gyr increases with ρ_h as $\mathcal{M}_p \propto \rho_h^{0.41\pm0.10}$ or $\mathcal{M}_p \propto \rho_h^{0.44\pm0.10}$ when using the prescriptions for mass loss due to two-body relaxation by MF08 or BM03, respectively. While this dependence of $\mathcal{M}_p$ on ρ_h is consistent with that found for the (old) blue GCs in NGC 1316 as well as

for the GC systems of the Milky Way and the Sombrero galaxy as mentioned above, we emphasize that it is *not only due to internal two-body relaxation for the red GCs in NGC 1316*. With this in mind, we suggest that disruption of low-density "supertidal" GCs by tidal shocks may be partly responsible for this scaling relation among MFs of ancient GC systems.

6.3. *The Nature of Diffuse Red Clusters*

Finally, we comment on the nature and demography of the class of diffuse red clusters, which are quite prevalent in NGC 1316. Diffuse clusters with properties (luminosities, colors, sizes) similar to those found here in NGC 1316 were first introduced as "faint fuzzies" by Larsen & Brodie (2000) and are also sometimes referred to as "extended clusters" (Huxor et al. 2008). While extended clusters are also found in halos of nearby spiral galaxies and in dwarf galaxies, the great majority of the latter are metal-poor (Chandar et al. 2004; Huxor et al. 2008; Georgiev et al. 2009, and references therein), whereas diffuse clusters found in NGC 1316 and younger merger remnants are metal-rich. We therefore constrain the following discussion to the case of *metal-rich* diffuse GCs, i.e., diffuse GCs with $(V-I)_0 \gtrsim 1.05$ or $(g-z)_0 \gtrsim 1.10$, similar to the "faint fuzzies" originally introduced by Larsen & Brodie (2000) and the "diffuse star clusters" discussed by Peng et al. (2006b). Here we adopt the acronym DRC ("diffuse red clusters") to describe this class of objects.

As shown by Larsen et al. (2001) and Peng et al. (2006b), "normal" giant early-type galaxies that are known to host significant numbers of DRCs share a number of properties that seem relevant to the nature of DRCs: *(i)* Their morphological type is virtually always S0 rather than E; *(ii)* They exhibit various signatures of ongoing or past interactions with neighboring galaxies such as strong fine structure, disturbed morphology, the presence of companion spiral galaxies, or their location as the dominant galaxy of a small galaxy group. In contrast, giant S0 galaxies in the samples of Larsen et al. (2001) and Peng et al. (2006b) that do not show such signatures of past interactions do not possess any significant number of DRCs. This observation is consistent with the suggestion by Brüns et al. (2009, 2011, and references therein) that such diffuse clusters may be formed by merging of star cluster complexes such as those commonly found in starburst regions within galaxy mergers or in the disks of giant spiral galaxies (e.g. Bastian et al. 2005). The fact that NGC 1316 possesses a large number of DRCs also corroborates this idea, given its nature as an obvious merger remnant and its dynamical nature as a rotationally supported galaxy (similar to S0 galaxies).

Several properties of DRCs are consistent with their denser counterparts (i.e., red GCs of "normal" size, $1 \lesssim r_h/\mathrm{pc} \lesssim 7$), which may help further our understanding of their nature. The spatial distribution of DRCs in S0 galaxies typically follows that of the galaxy light: It is very elongated for "late-type" S0s such as NGC 1023 and NGC 3384 (Larsen & Brodie 2000), and more spherical for bulge-dominated S0s such as M85 (Peng et al. 2006b) as well as NGC 1316 (see Sect. 5.2). Apart from their apparent absence in the innermost regions of galaxies, the DRCs seem to be similar in this respect to "normal" red GCs, which are typically closely associated with the bulge component of their host galaxy as well (e.g., Kissler-Patig et al. 1997; Goudfrooij et al. 2001a, 2007; Peng et al. 2006a). In the scenario where the red GCs and the bulges of early-type galaxies are formed during dissipative galaxy mergers, this physical association indicates that the progeni-

tors of the red GCs underwent the same violent relaxation as did the stars of the progenitor galaxies.

The main difference between DRCs and "normal" red GCs within a given normal galaxy (apart from their sizes) is that DRCs typically have masses lower than the mass associated with the typical turnover magnitude of the GCLF of "normal" red GCs (Brodie & Larsen 2002; Peng et al. 2006b). This is the case in NGC 1316 as well, although the DRCs in NGC 1316 reach slightly higher masses, perhaps due to their younger age which renders their masses to be closer to their initial masses. This difference in mass ranges is relevant because the formation efficiency of young massive clusters in a certain region has been shown to scale with the star formation rate (SFR) in that region (Larsen & Richtler 2000). This correlation is likely a consequence of the correlations between SFR and gas density (Kennicutt 1998) and between gas density and the star formation efficiency in high-mass clouds (Efremov 1994; Elmegreen & Efremov 1997). Hence, the number of GCs of a certain class above a certain mass threshold should be proportional to the SFR at the time those GCs were formed (see also Larsen 2002; Weidner et al. 2004; Bastian 2008; Georgiev et al. 2012). Since it is hard to preferentially destroy massive GCs while preserving low-mass ones, we suggest that the typically lower masses of DRCs with respect to "normal" red GCs reflects that the DRCs were formed in *sites with lower SFR* than in the formation sites of the "normal" GCs. Perhaps DRCs are formed in gas clouds with relatively low density with respect to the clouds that produce normal GCs. This is consistent with the suggestion by Elmegreen (2008) that DRCs are formed in clouds that are at or near the low-density limit for cluster boundedness in regions with high turbulence (Mach numbers). Such circumstances can likely occur in galaxy mergers by means of shocked clouds or direct ISM impacts between components of the progenitor galaxies, perhaps mainly outside the inner, dynamically most violent region of the interaction.

Incidently, such a scenario of environment-driven formation of DRCs may also explain why DRCs seem to be largely absent in giant E galaxies (as opposed to S0 galaxies). According to the extensive N-body/hydro simulations of Mihos & Hernquist (1996), mergers of two early-type disk galaxies (i.e., galaxies with significant bulge components) typically experience peak SFRs that are factors $2-5$ higher than do mergers of two late-type disk galaxies (without bulges),

with the value of the factor depending on the geometry of the galaxy encounters. Perhaps the assembly histories of giant E galaxies with their pressure-supported stellar dynamics were dominated by interactions involving progenitor galaxies with pre-existing bulge components, while rotation-supported giant S0 galaxies may have been assembled mainly (or more predominantly) by means of interactions involving bulgeless disk galaxies. The lower gas densities achieved in the latter interactions may have triggered the formation of several DRCs whereas the high-SFR interactions between galaxies with pre-existing bulges may not have.

In the context of this scenario, the absence of DRCs in many giant S0 galaxies may be due to gradual disruption of DRCs by tidal shocks as discussed above for NGC 1316. The DRCs seen in some S0 galaxies may have been formed during relatively recent dissipative interactions of galaxies that did not host significant bulges. Looking at Figure 16b, "relatively recent" in this context would mean less than roughly $7-9$ Gyr ago for a galaxy with a mass similar to NGC 1316, and possibly longer ago for less massive galaxies. For most giant early-type galaxies however, such interactions have likely happened long enough ago for the DRCs to have suffered enough mass loss to be rendered undetectable (or too faint to obtain reliable size information) at the present day, at least in their inner regions which were typically targeted by the *HST* observations. Time will tell whether DRCs can (still) be detected and identified in the tidally benign outer regions of giant early-type galaxies.

REFERENCES

Anderson, J., & King, I. R. 2006, "PSFs, Photometry, and Astrometry for the ACS/WFC", ACS Instrument Science Report 2006-01 (Baltimore:STScI)

Arnaboldi, M., Freeman, K. C., Gerhard, O., et al. 1998, ApJ, 507, 759

Ashman, K. M., & Zepf, S. E. 1992, ApJ, 384, 50

Bastian, N. 2008, MNRAS, 390, 759

Bastian, N., Gieles, M., Efremov, Yu. N., & Lamers, H. J. G. L. M. 2005, A&A, 443, 79

Bastian, N., Saglia, R. P., Goudfrooij, P., et al. 2006, A&A, 448, 881

Bastian, N., Gieles, M., Goodwin, S. P., et al. 2008, MNRAS, 389, 223

Bastian, N., Trancho, G., Konstantopoulos, I. S., & Miller, B. W. 2009, ApJ, 701, 607

Baugh, C. M., Cole, S., & Frenk, C. S. 1996, MNRAS, 283, 1361

Baumgardt, H., & Makino, J. 2003, MNRAS, 340, 227 (BM03)

Baumgardt, H., & Kroupa, P. 2007, MNRAS, 380, 1589

Baumgardt, H., Kroupa, P., & Parmetier, G. 2008, MNRAS, 384, 1231

Bender, R. 1988, A&A, 193, L7

Binney, J., & Tremaine, S. 1987, Galactic Dynamics (Princeton, NJ: Princeton University Press)

Brodie, J. P., & Larsen, S. S. 2002, AJ, 124, 1410

Brodie, J. P., Schroder, L. L., Huchra, J. P., Phillips, A. C., Kissler-Patig, M., & Forbes, D. A. 1998, AJ, 116, 691

Brüns, R. C., Kroupa, P., & Fellhauer, M. 2009, ApJ, 702, 1268

Brüns, R. C., Kroupa, P., Fellhauer, M., Metz, M., & Assmann, P. 2011, A&A, 529, A138

Bruzual, G. A., & Charlot, S. 2003, MNRAS, 344, 1000 (BC03)

Burkert, A., & Smith, G. H. 2000, ApJ, 542, L95

Caon, N., Capaccioli, M., & D'Onofrio, M., 1994, A&AS, 106, 199

Carlson, M. N., & Holtzman, J. A. 2001, PASP, 113, 1522

Chabrier, G. 2003, PASP, 115, 763

Chandar, R., Whitmore, B. C., & Lee, M. G. 2004, ApJ, 611, 220

Chandar, R., Fall, S. M., & McLaughlin, D. E. 2007, ApJ, 668, L119

Cole, S., Lacey, C. G., Baugh, C. M., & Frenk, C. S. 2000, MNRAS, 319, 168

Dehnen, W., Odenkirchen, M., Grebel, E. K., & Rix, H.-W. 2004, AJ, 127, 2753

de Vaucouleurs, G. et al., 1991, "Third Reference Catalog of Bright Galaxies" (New York: Springer)

Efremov, Yu. N. 1994, in Violent Star Formation from 30 Dor to QSOs, ed. G. Tenorio-Tagle (Cambridge: Cambridge University Press), 61

Elmegreen, B. G. 2008, ApJ, 672, 1006

Elmegreen, B. G., & Efremov, Yu. N. 1997, ApJ, 480, 235

Fall, S. M., & Rees, M. J. 1977, MNRAS, 181, 37P

Fall, S. M., & Zhang, Q. 2001, ApJ, 561, 751

Fall, S. M., Chandar, R., & Whitmore, B. C. 2009, ApJ, 704, 453

Forbes, D. A., Brodie, J. P., & Grillmair, C. J. 1997, AJ, 113, 1652

Forbes, D. A., Beasley, M. A., Brodie, J. P., & Kissler-Patig, M. 2001, ApJ, 563, L143

Geisler, D., Lee, M. G., & Kim, E. 1996, AJ, 111, 1529

Georgiev, I. Y., Puzia, T. H., Hilker, M., & Goudfrooij, P. 2009, MNRAS, 392, 879

Georgiev, I. Y., Goudfrooij, P., & Puzia, T. H. 2012, MNRAS, 420, 1317

Gieles, M., & Baumgardt, H. 2008, MNRAS, 389, L28

Gieles, M., Larsen, S. S., Bastian, N., & Stein, I. T. 2006, A&A, 450, 129

Giersz, M., & Heggie, D. C. 1996, MNRAS, 279, 1037

Gnedin, O. Y., & Ostriker, J. P. 1997, ApJ, 474, 223

Gnedin, O. Y., Lee, H. M., & Ostriker, J. P. 1999, ApJ, 522, 935

Goudfrooij, P., Alonso, M. V., Maraston, C., & Minniti, D. 2001a, MNRAS, 328, 237

Goudfrooij, P., Mack, J., Kissler-Patig, M., Meylan, G., & Minniti, D. 2001b, MNRAS, 322, 643

Goudfrooij, P., Gilmore, D., Whitmore, B. C., & Schweizer, F. 2004, ApJ, 613, L121

Goudfrooij, P., Schweizer, F., Gilmore, D., & Whitmore, B. C., 2007, AJ, 133, 2737

Harris, W. E. 1996, AJ, 112, 1487

Harris, W. E. 2001, in Star Clusters, ed. L. Labhardt & B. Binggeli (Berlin:Springer), 223

Harris, W. E. 2009, ApJ, 699, 254

Heggie, D. C., & Giersz, M. 2008, MNRAS, 389, 1858

Holtzman, J. A., Faber, S. M., Shaya, E. J., et al. 1992, AJ, 103, 691

Huxor, A. P., Tanvir, N. R., Ferguson, A. M. N., Irwin, M. J., Ibata, R., Bridges, T., & Lewis, G. F. 2008, MNRAS, 385, 1989

Hwang, N., & Lee, M. G. 2006, ApJ, 638, L79

Jordán, A., Côté, P., West, M. J., Marzke, R. O., Minniti, D., & Rejkuba, M. 2004, AJ, 127, 24

Jordán, A., et al. 2005, ApJ, 634, 1002

Jordán, A., et al. 2007, ApJS, 171, 101

Kennicutt Jr., R. C. 1998, ApJ, 498, 541

King, I. R. 1962, AJ, 67, 471

Kissler-Patig, M., Richtler, T., Storm, J., & della Valle, M. 1997, A&A, 327, 503

Krist, J., & Hook, R. 2004, The TINY TIM Manual (http://www.stsci.edu/software/tinytim/tinytim.html)

Kroupa, P. 2001, MNRAS, 322, 231

Kruijssen, J. M. D., Pelupessy, F. I., Lamers, H. J. G. L. M., Portegies Zwart, S. F., Bastian, N., & Icke, V. 2011, MNRAS, 414, 1339

Kundu, A. 2008, AJ, 136, 1013

Kundu, A., & Whitmore, B. C. 1998, AJ, 116, 2841

Kundu, A., & Whitmore, B. C. 2001, AJ, 121, 1888

Lada, C. J., & Lada, E. A. 2003, ARA&A, 41, 57

Larsen, S. S. 1999, A&AS, 139, 393

Larsen, S. S. 2002, AJ, 124, 1393

Larsen, S. S., & Brodie, J. P. 2000, AJ, 120, 2938

Larsen, S. S., & Richtler, T. 2000, A&A, 354, 836

Larsen, S. S., Brodie, J. P., Huchra, J. P., Forbes, D. A., & Grillmair, C. J. 2001, AJ, 121, 2974

Mackey, A. D., Wilkinson, M. I., Davies, M. B., & Gilmore, G. F. 2008, MNRAS, 386, 65

Madrid, J. P., Harris, W. E., Blakeslee, J. P., & Gómez, M. 2009, ApJ, 705, 237

Marín-Franch, A., et al. 2009, ApJ, 694, 1498

Masters, K. L., Jordán, A., Côté, P., et al. 2010, ApJ, 715, 1419

Maraston, C. 2005, MNRAS, 362, 799

Maraston, C., Kissler-Patig, M., Brodie, J. P., Barmby, P., & Huchra, J. P., 2001, A&A, 370, 176

Maraston, C., Bastian, N., Saglia, R. P., Kissler-Patig, M., Schweizer, F., & Goudfrooij, P. 2004, A&A, 416, 467

McLaughlin, D. E. 2000, ApJ, 539, 618

McLaughlin, D. E., & Fall, S. M. 2008, ApJ, 679, 1272 (MF08)

McLaughlin, D. E., & Pudritz, R. E. 1996, ApJ, 469, 194

McLaughlin, D. E., & van der Marel, R. P. 2005, ApJS, 161, 304

Meurer, G. R., Heckman, T. M., Leitherer, C., Kinney, A., Robert, C., & Garnett, D. R. 1995, AJ, 110, 2665

Mihos, J., & Hernquist, L. 1996, ApJ, 464, 641

Miller, B. W., Whitmore, B. C., Schweizer, F., & Fall, S. M. 1997, AJ, 114, 2381

Odenkirchen, M., et al. 2003, AJ, 126, 2385

Paolillo, M., Puzia, T. H., Goudfrooij, P., et al. 2011, ApJ, 736, 90

Peng, E. W., Jordán, A., Côté, P., et al. 2006, ApJ, 639, 95

Peng, E. W., Côté, P., Jordán, A., et al. 2006, ApJ, 639, 838

Portegies Zwart, S. F., McMillan, S. L. W., & Gieles, M. 2010, ARA&A, 48, 431

Prieto, J. L., & Gnedin, O. Y. 2008, ApJ, 689, 919

Puzia, T. H., Kissler-Patig, M., Brodie, J. P., & Huchra, J. P. 1999, AJ, 118, 2734

Puzia, T. H., Kissler-Patig, M., Thomas, D., Maraston, C., Saglia, R. P., Bender, R., Goudfrooij, P., & Hempel, M. 2005, A&A, 439, 997

Puzia, T. H., Kissler-Patig, M., & Goudfrooij, P. 2006, ApJ, 648, 383

Puzia, T. H., Paolillo, M., Goudfrooij, P., et al. 2012, in preparation

Rhode, K. L., & Zepf, S. E. 2001, AJ, 121, 210

Salpeter, E. E. 1955, ApJ, 121, 161

Sandage, A. R., & Tammann, G. A. 1987, "A Revised Shapley-Ames Catalog of Bright Galaxies" (Washington: Carnegie Institution of Washington)

Schechter, P. 1976, ApJ, 203, 297

Schweizer, F. 1980, ApJ, 237, 303

Schweizer, F. 1981, ApJ, 246, 722

Schweizer, F. 1987, in: "Nearly Normal Galaxies", ed. S. M. Faber (Springer: New York), 18

Schweizer, F., & Seitzer, P. 1998, AJ, 116, 2206

Schweizer, F., Miller, B. W., Whitmore, B. C., & Fall, S. M. 1996, AJ, 112, 1839

Sirianni, M. et al. 2005, PASP, 117, 1049

Somerville, R. S., Primack, J. R., & Faber, S. M. 2001, MNRAS, 320, 504

Spitler, L. R., Larsen, S. S., Strader, J., et al. 2006, AJ, 132, 1593

Spitzer, L. 1987, Dynamical Evolution of Globular Clusters (Princeton: Princeton University Press)

Toomre, A. 1977, in The Evolution of Galaxies and Stellar Populations, ed. B. Tinsley & R. Larson (New Haven: Yale University Press), 401

Trancho, G., Bastian, N., Schweizer, F., & Miller, B. W. 2007, ApJ, 658, 993

Venables, W. N., & Ripley, B. D. 2002, Modern Applied Statistics with S (New York: Springer)

Vesperini, E. 2000, MNRAS, 318, 841

Vesperini, E. 2001, MNRAS, 322, 247

Vesperini, E., McMillan, S. L. W., & Portegies Zwart, S. 2009, ApJ, 698, 615

Weidner, C., Kroupa, P., & Larsen, S. S. 2004, MNRAS, 350, 1503

White, S. D. M., & Frenk, C. S. 1991, ApJ, 379, 52

Whitmore, B. C., Zhang, Q., Leitherer, C., Fall, S. M., Schweizer, F., & Miller, B. W. 1999, AJ, 118, 1551

Whitmore, B. C., Schweizer, F., Kundu, A., & Miller, B. W. 2002, AJ, 124, 147

Whitmore, B. C., Chandar, R., Schweizer, F., et al. 2010, AJ, 140, 75

Woodley, K. A., Harris, W. E., Puzia, T. H., Gómez, M., Harris, G. L. H., & Geisler, D. 2010, ApJ, 708, 1335

Zepf, S. E., Carter, D., Sharples, R. M., Ashman, K. M. 1995, ApJ, 445, L19

Zepf, S. E., Ashman, K. M., English, J., Freeman, K. C., & Sharples, R. M. 1999, AJ, 118, 752

Zhang, Q., & Fall, S. M. 1999, ApJ, 527, L81

TABLE 2
PROPERTIES OF EVOLVED SCHECHTER FUNCTION FITS TO CLUSTER SAMPLES.

Sample (1)	Subsample (2)	$\widetilde{\rho}_{\rm h}$ (3)	$\widetilde{\Delta}$ (4)	$\mathcal{M}_{\rm p}$ (5)
Blue, $V < 25.3$	all	164	1.0×10^5	8.4×10^4
	low-$\rho_{\rm h}$ bin	36	5.5×10^4	5.0×10^4
	high-$\rho_{\rm h}$ bin	1317	2.7×10^5	1.9×10^5
	inner $R_{\rm gal}$ bin	229	1.1×10^5	9.1×10^4
	outer $R_{\rm gal}$ bin	120	7.0×10^4	6.2×10^4
Red (now), $V < 25.3$	low-$\rho_{\rm h}$ bin	6	6.2×10^3	6.2×10^3
	high-$\rho_{\rm h}$ bin	274	4.4×10^4	4.4×10^4
	inner $R_{\rm gal}$ bin	42	1.7×10^4	1.7×10^4
	outer $R_{\rm gal}$ bin	10	8.4×10^3	8.4×10^3
Red (13 Gyr, MF08), $V < 25.3$	all	16	1.0×10^5	9.1×10^4
	low-$\rho_{\rm h}$ bin	4	6.0×10^4	5.7×10^4
	high-$\rho_{\rm h}$ bin	213	1.5×10^5	1.3×10^5
	inner $R_{\rm gal}$ bin	115	1.1×10^5	1.0×10^5
	outer $R_{\rm gal}$ bin	9	8.3×10^4	7.7×10^4
Red (13 Gyr, BM03), $V < 25.3$	all	11	8.0×10^4	7.3×10^4
	low-$\rho_{\rm h}$ bin	3	3.2×10^4	3.1×10^4
	high-$\rho_{\rm h}$ bin	283	1.5×10^5	1.3×10^5
	inner $R_{\rm gal}$ bin	97	1.1×10^5	1.0×10^5
	outer $R_{\rm gal}$ bin	6	6.1×10^4	5.7×10^4
Red (13 Gyr, MF08), $V < 25.8$	low-$\rho_{\rm h}$ bin	3	3.4×10^4	3.3×10^4
	high-$\rho_{\rm h}$ bin	115	1.5×10^5	1.3×10^5
	inner $R_{\rm gal}$ bin	35	1.0×10^5	9.1×10^4
	outer $R_{\rm gal}$ bin	7	4.9×10^4	4.7×10^4
Red (13 Gyr, BM03), $V < 25.8$	low-$\rho_{\rm h}$ bin	2	2.1×10^4	2.0×10^4
	high-$\rho_{\rm h}$ bin	125	1.3×10^5	1.1×10^5
	inner $R_{\rm gal}$ bin	26	9.0×10^4	0.8×10^5
	outer $R_{\rm gal}$ bin	5	4.3×10^4	4.1×10^4

NOTE. — Column (1): Star cluster sample and limiting V magnitude. 'MF08' and 'BM03' refer to models used to apply 10 Gyr of dynamical evolution to the cluster sample in question. Only surviving clusters are considered. See discussion in §§ 4.4 and 5.3. (2): Star cluster subsample. (3): Median half-mass density in $M_\odot$ pc^{-3}. (4): Median of best-fit mass lost per cluster in $M_\odot$. The typical formal uncertainty of $\widetilde{\Delta}$ returned by the fits is $\sim 25\%$. (5) Peak mass associated with turnover of luminosity function, in $M_\odot$.